Chemical Geology 576 (2021) 120231

Contents lists available at ScienceDirect

Chemical Geology

journal homepage: www.elsevier.com/locate/chemgeo

The Molybdenum isotope subduction recycling conundrum: A case study from the Tongan subduction zone, Western Alps and Alpine Corsica

Qasid Ahmad [a,*], Martin Wille [a], Stephan König [b], Carolina Rosca [b], Angela Hensel [a], Thomas Pettke [a], Jörg Hermann [a]

[a] Institute of Geological Sciences, University of Bern, Switzerland
[b] Isotope Geochemistry, Department of Geosciences, University of Tübingen, Germany

ARTICLE INFO

Editor: Balz Kamber

ABSTRACT

Molybdenum isotopes have emerged as novel tracers for high-temperature igneous and metamorphic processes. The debate remains to what extent different subducted slab lithologies, such as oceanic crust and marine sediments, contribute to the Mo isotope signature of arc magmas and, hence, exert different controls on the terrestrial Mo cycle. Here we investigate Mo isotope systematics from input to output at the Tongan subduction zone: Arc lavas from different Tongan islands, pelagic sediments and altered oceanic crust (AOC) samples from DSDP site 595/596 on the subducting Pacific plate. For complementary insights into the fate of Mo and its isotopic signatures during prograde subduction metamorphism, we also present data of metasediments and variably altered AOC-type eclogites from the Zermatt-Saas ophiolite, Switzerland and Italy, and the Schistes Lustrés Complex in Alpine Corsica.

Manganese oxide-rich pelagic sediments from DSDP site 595/596 show variable, depth-dependent Mo/Mn ratios and Mo isotope compositions controlled by diagenetic reactions. As subducted equivalents, Mn-rich eclogitic metapelites display lower Mo contents and $\delta^{98/95}$Mo ratios compared to their non-subducted protolith. This indicates prominent loss of Mo along with isotope fractionation during early subduction metamorphism. In comparison to unaltered MORB, low temperature seafloor alteration has shifted Mo/Ce and $\delta^{98/95}$Mo in studied AOC samples towards lower ratios, in the range of most mafic eclogites published so far. However, some mafic eclogites show even lower Mo/Ce and $\delta^{98/95}$Mo ratios compared to AOC, likely due to fluid-related Mo loss upon early subduction and preferential incorporation of light Mo into residual rutile.

Our data document a prominent loss of isotopically heavy Mo before and upon early subduction metamorphism at shallow depths in the forearc region. Moreover, when prograde rutile crystallizes at ~30 km depth, it fixes the largest fraction of Mo in the subducting material. This creates an "arc Mo-conundrum" as devolatization of the slab at subarc depths is not able to account for the fluid-mobile Mo source responsible for observed higher Mo/Ce and $\delta^{98/95}$Mo in Tongan arc lavas compared to the mantle. As an alternative scenario, Mo mobilization by slab-derived aqueous fluids during the early stages of subduction into the forearc mantle produces serpentinites enriched in Mo with a possible heavy Mo isotopic signature. Mechanical transport and devolatization of forearc serpentinites at subarc regions is a plausible alternative recycling process accounting for the observed Mo systematics in Tongan arc lavas. This is supported by positive covariations of Mo/Ce and $\delta^{98/95}$Mo with elements such as As, Sb, and Cs, which are thought to be mostly released from the subducting material during early stages of subduction. We propose that a multi-stage recycling of metasomatized forearc mantle can be an important process in recycling of Mo and possibly other elements.

1. Introduction

Subduction zone magmatism at convergent margins is closely associated with the formation of continental crust. These settings are characterized by high mass fluxes between oceanic crust and mantle, where slab-derived fluids (aqueous fluids or hydrous melts) facilitate the element transfer into the mantle wedge (Hermann et al., 2006). Molybdenum has been shown to be mobile in subduction zone fluids (König

* Corresponding author at: Isotope Geology Group, Institute of Geological Sciences, University of Bern, Baltzerstrasse 1+3, CH-3012 Bern, Switzerland.
E-mail address: qasid.ahmad@geo.unibe.ch (Q. Ahmad).

https://doi.org/10.1016/j.chemgeo.2021.120231
Received 28 November 2020; Received in revised form 31 March 2021; Accepted 7 April 2021
Available online 16 April 2021

et al., 2010; König et al., 2008) and experimental constraints indicate that this mobility is controlled by the redox state and salinity of hydrous fluids involved (Bali et al., 2012; Skora et al., 2017). In recent years, stable Mo isotope ratios, expressed as $\delta^{98/95}Mo_{SRM3134}$ (herein: $\delta^{98/95}Mo$), have been applied to investigate the slab-mantle wedge transport and ultimately the incorporation of this element into arc lavas (Casalini et al., 2019; Chen et al., 2019; Freymuth et al., 2016; Freymuth et al., 2015; Gaschnig et al., 2017; König et al., 2016; Villalobos-Orchard et al., 2020; Zhang et al., 2020).

Present-day aqueous Mo mobilization and transformation processes induce a large variability in Mo concentrations and isotope signatures in different marine sediments ($\delta^{98/95}Mo = -0.9$ to $+2.1$‰; e.g., Barling et al., 2001; Freymuth et al., 2016, Freymuth et al., 2015; Gaschnig et al., 2017; Kendall et al., 2017; Siebert et al., 2003) compared to the homogeneous signature of the depleted mantle with $\delta^{98/95}Mo$ of -0.2‰ (McCoy-West et al., 2019). Manganese-rich pelagic sediments constitute one isotopically light sedimentary endmember; hence, they are of particular interest to study the element recycling in subduction zones with Mo isotopes. This lithology is highly enriched in Mo and has a light Mo isotopic composition, down to $\delta^{98/95}Mo = -0.9$‰, due to isotopic fractionation during Mo scavenging from seawater ($\delta^{98/95}Mo = +2.1$‰) onto Mn-oxides (Barling et al., 2001; Barling and Anbar, 2004; Siebert et al., 2003). Anoxic sediments, such as black shales primarily deposited at continental margins, also show a large Mo isotopic range, with generally higher $\delta^{98/95}Mo$ than the depleted mantle and up to the seawater Mo isotopic composition (e.g., Barling et al., 2001; Gordon et al., 2009; Siebert et al., 2003). Thus, the recycling of isotopically variable Mo during sediment subduction can be potentially traced in arc volcanic rocks. Indeed, direct recycling of sediments during subduction has been suggested to affect the Mo isotope signature of arc lavas (Casalini et al., 2019; Freymuth et al., 2016; Gaschnig et al., 2017; Zhang et al., 2020). A sediment melt contribution of isotopically heavy black shales has been proposed to explain the heavy Mo isotopic composition of arc lavas from the Lesser Antilles arc (Freymuth et al., 2016).

Higher $\delta^{98/95}Mo$ signatures compared to the depleted mantle have also been observed in arc lavas from the Mariana arc (Freymuth et al., 2015), Solomon arc (König et al., 2016) and Izu arc (Villalobos-Orchard et al., 2020), which are recognized as aqueous, slab-fluid dominated subduction zone settings. These signatures were attributed to the formation of secondary minerals during subduction metamorphism, which preferentially incorporate light Mo, leading to an isotopically heavy slab-derived fluid that enters the mantle wedge. Chen et al. (2019) analyzed the Mo isotopic composition of a suite of blueschists and MORB-type eclogites and found overall lower $\delta^{98/95}Mo$, ranging from -0.13 to -0.99‰ compared to that of mantle/MORB values -0.16 to -0.22‰ (Bezard et al., 2016; Burkhardt et al., 2014; Greber et al., 2015; Liang et al., 2017; McCoy-West et al., 2019). This light bulk rock Mo isotopic composition goes along with lower Mo/Ce ratios indicating a loss of Mo from eclogites. Chen et al. (2019) could further show that rutile, a major host of Mo in eclogites, preferentially incorporates light Mo with individual rutile grains in eclogites showing even lower $\delta^{98/95}Mo$ (-0.31 to -1.26‰) than the bulk eclogites. Consequently, these authors argue that rutile formation and concurrent loss of Mo by oxidized fluid flow through the oceanic crust, with the dominant aqueous fluid source being the underlying serpentinized mantle, produces the complementary heavy Mo isotopic signature in fluids entering the mantle wedge. Subsequent melting of residual rutile hosted in e.g. sedimentary mélange recycles the isotopically light Mo into the subarc mantle wedge, as proposed to explain the isotopically light arc lavas with $\delta^{98/95}Mo$ down to -0.8‰ found in Cyprus and Papua New Guinea (König et al., 2016).

Fractional crystallization of hydrous minerals such as biotite and amphibole, which preferentially incorporate light Mo, has also been suggested to explain an isotopically heavy residual melt (Voegelin et al., 2014; Wille et al., 2018), while anhydrous differentiation has no significant effect onto the Mo isotope signature (Bezard et al., 2016; McCoy-West et al., 2019; Yang et al., 2015). This commonly suggests that the rather large $\delta^{98/95}Mo$ heterogeneity of primitive arc lavas (i.e. with >5 wt% MgO) comprises the sum of the Mo isotope signature of the subducted lithologies plus intrinsic processes (i.e. subduction metamorphism) that influence the mantle Mo budget and its isotopic composition.

To better constrain to what extent different subducted lithologies may contribute to the Mo isotope signature of arc lavas, we investigated the Mo isotope systematics at the Tongan subduction zone (Fig. 1). The Tongan arc represents a valuable endmember to study Mo recycling in intra-oceanic subduction zones because of Mn-rich pelagic sediment subduction, one of the fastest convergence rates, coldest slab temperatures, and most depleted subarc mantle wedges worldwide (e.g., Bevis et al., 1995; Menard et al., 1987; Plank, 2005; Syracuse et al., 2010). Samples include pelagic clays from the Deep Sea Drilling Project (DSDP) site 595/596 (~5600–5700 m below sea level), which are compared with subducted analogues comprising Mn-rich pelitic metasediments from Zermatt-Saas ophiolite and Lago di Cignana in the Western Alps, and the Schistes Lustrés Complex in Alpine Corsica. Altered oceanic crust (AOC) samples from the same DSDP site are compared with exhumed AOC-type eclogites from Zermatt-Saas ophiolite and Tongan arc lavas. Analyzed exhumed metamorphic rocks experienced a wide range of peak metamorphic pressure and temperature conditions (Fig. 2) and offer insight into the nature of Mo mobility and isotope fractionation during subduction.

2. Geological setting and sample material

2.1. Tongan arc and DSDP site 595/596

Molybdenum isotope analyses were performed on a subset of 27 arc lavas (basalts to basaltic andesites), from a larger sample set collected on the uninhabited Tongan volcanic islands of Late, Tofua, Kao, and Ata in May 2017. The ~1500 km Tongan island arc is situated along a convergent margin in the southwest Pacific Ocean and is separated from the Kermadec arc to the south by the Louisville seamount chain (LSC) and to the north by the Vitiaz trench. The main Tongan arc formed by the subduction of the Jurassic-Cretaceous Pacific Plate beneath the Australian Plate since the Oligocene (e.g., Turner et al., 1997), a common feature in the evolution of many island arcs in the SW Pacific plate

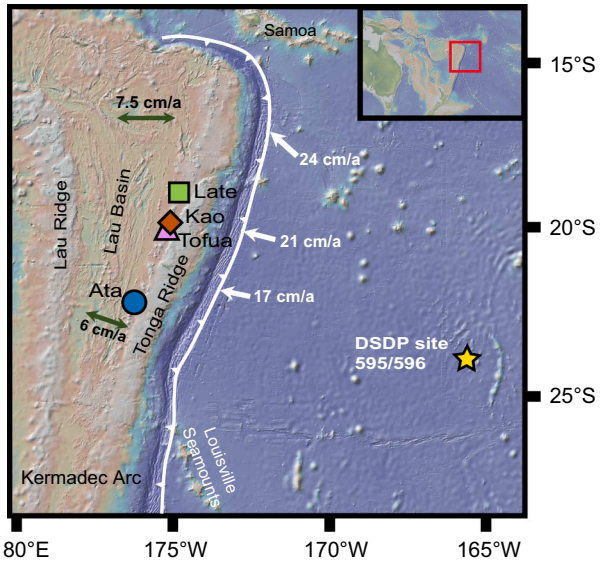

Fig. 1. Map showing investigated Tongan arc islands of Late, Kao, Tofua and Ata and the DSDP site 595/596 together with convergence and spreading rates from Bevis et al. (1995). Figure made with GeoMapApp (www.geomapapp.org).

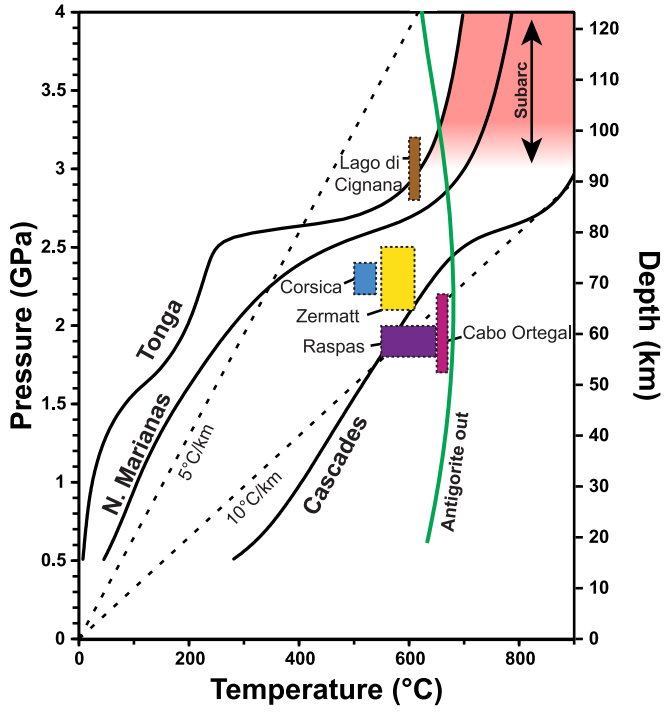

Fig. 2. Pressure-temperature diagram displaying estimated peak-metamorphic conditions of studied metasediments and AOC-type eclogites from Zermatt, Lago di Cignana, and Corsica and corresponding approximate depth of subduction. For comparison, peak P-T conditions of blueschists and MORB-type eclogites from Cabo Ortegal and Raspas are displayed (Chen et al., 2019, and references therein). The stability of antigorite is shown for reference (Ulmer and Trommsdorff, 1995) together with modeled P-T paths of the slab surface of Tonga (D80 model of Syracuse et al. (2010)). Models of North Marianas and Cascades (Syracuse et al., 2010) exemplify intermediate and hot subduction zones, respectively.

border region (e.g., Schuth et al., 2011). There is a northwards increase in convergence and backarc spreading rates along the arc (Fig. 1; Bevis et al., 1995), resulting in increasing relative mantle depletion northwards (Escrig et al., 2009; Ewart et al., 1998). High convergence rates and the subduction of old oceanic lithosphere led to one of the coldest subduction zones (e.g., Wei et al., 2017). Pleistocene to recent arc volcanic rocks of the Tongan islands are mainly of tholeiitic and basaltic andesite composition with minor occurrences of andesites and dacites (Caulfield et al., 2012, and references therein).

In addition to the arc lavas, 24 sample cuts (14 sediment samples and 10 AOC samples) covering the entire sampling depth of the DSDP site 595/596 core (~120 m below seafloor) were analyzed. It has been proposed that the overall subduction input into the Tongan mantle source consists mainly of AOC- and sediment-derived aqueous fluid and a hydrous sediment melt, while in the southern part additional contributions of volcanoclastic sediments from the LSC occur (Escrig et al., 2009). The sediment layer from the DSDP sites 595/596 has a thickness of only ~70 m. It consists of pelagic clays rich in ferromanganese oxides, with biogenic silica and porcellanite-rich layers in the bottom overlying N-MORB type AOC (Menard et al., 1987; Zhou and Kyte, 1992). The alteration of the basaltic crust corresponds to the lower temperature oxidation stage 5 of Johnson and Hall (1978) forming titanomaghemite from titanomagnetite, and the subsequent formation of alteration minerals like Fe-oxyhydroxides (Menard et al., 1987). The alteration is expressed by carbonate veins formed at low temperature (13–23 °C) consisting of Fe-oxyhydroxides and in part smectite (Gillis and Coogan, 2011; Menard et al., 1987). Due to the remoteness from continental shelf areas, pelagic clays, instead of terrigenous sediments, dominate the sedimentary subduction input (Menard et al., 1987). The absence of an accretionary wedge at the trench shows that the sediment is not physically eroded during subduction (Ballance et al., 1989; Clift and Vannucchi, 2004). Furthermore, the Tongan arc exhibits an extremely depleted mantle wedge signature in comparison to other arcs (e.g., based on relative high Sm/La ratios observed in arc lavas; Plank, 2005) invoking the possibility that already minor contributions of slab-derived, incompatible elements can be traced in the composition of arc magmas. Also, Leeman et al. (2017) argued that melt production in the Tongan arc is proportional to the overall fluid flux beneath the arc, which explains the depleted nature of the subarc setting, especially at Tofua where the highest slab-derived aqueous fluid flux within the arc is observed (e.g., Caulfield et al., 2012).

2.2. Western Alps & Corsica

A total of 9 exhumed metasedimentary rocks from the Zermatt-Saas Unit (Switzerland), Lago di Cignana (Italy), Alpine Corsica (France) and

Table 1
Sample location and mineralogy and peak P-T conditions of studied metamorphic rocks. See text for references.

Sample	Rock type	Mineralogy	P (GPa)	T (°C)
Pfulwe, Zermatt				
PF18-20	AOC-type eclogite	Glaucophane, Garnet, Epidote, Chlorite, Chloritoid, Paragonite, Rutile, Amphiboles	2.3 ± 0.2	580 ± 30
PF18-26	AOC-type eclogite	Chlorite, Glaucophane, Garnet, Talc, Paragonite, Chloritoid, Epidote, Rutile ± Sulfides	2.3 ± 0.2	580 ± 30
PF18-25a	AOC-type eclogite	Omphacite, Amphiboles, Paragonite, Garnet, Glaucophane, Epidote, Carbonate, Rutile	2.3 ± 0.2	580 ± 30
PF18-25c	AOC-type eclogite	Epidote, Quartz, Garnet, Rutile, Apatite, Paragonite ± Sulfides	2.3 ± 0.2	580 ± 30
Trockener Steg, Zermatt				
Z16TB31a	Grt-schist (clastic metasediment)	Quartz, White Mica, Zoisite, Garnet, Rutile ± Pyrite, Graphite	2.3 ± 0.2	580 ± 30
Z16TB31b	Grt-schist (clastic metasediment)	Quartz, White Mica, Zoisite, Garnet, Rutile ± Pyrite, Graphite	2.3 ± 0.2	580 ± 30
Z18TB20	Grt-schist (clastic metasediment)	Quartz, White Mica, Zoisite, Tourmaline, Amphiboles, Garnet, Rutile ± Carbonate	2.3 ± 0.2	580 ± 30
Lago di Cignana				
C13a	Mn-rich pelagic metasediment	Garnet, Omphacite, Quartz, Clinozoisite, Amphiboles, Epidote, Rutile ± Sulfides, Titanite	3.0 ± 0.2	610 ± 10
C13b	Mn-rich pelagic metasediment	Garnet, Omphacite, Quartz, Clinozoisite, Amphiboles, Epidote, Rutile ± Sulfides, Titanite	3.0 ± 0.2	610 ± 10
C11	Mn-rich pelagic metasediment	Quartz, Garnet, White Mica, Piemontite, Fe-Mn-oxides, Tourmaline ± Rutile	3.0 ± 0.2	610 ± 10
Schistes Lustrés Complex, Corsica				
COS 3	Mn-rich pelagic metasediment	Quartz, Piemontite, White Mica, Fe-Mn-oxides	2.3 ± 0.1	520 ± 20
COS 2	Mn-rich pelagic metasediment	Quartz, Garnet, White Mica, Rutile, Fe-Mn-oxides, Chlorite ± Graphite, Carbonate	2.3 ± 0.1	520 ± 20
COS 7	Clastic metasediment	Quartz, Lawsonite, White Mica, Chlorite, Graphite ± Fe-oxides, Titanite, Sulfides	2.3 ± 0.1	520 ± 20

4 AOC-type eclogites from Pfulwe (Zermatt, Switzerland) were analyzed (Table 1). These metamorphic rocks represent pelagic sediments and mafic oceanic crust, which attained variable peak P-T conditions upon convergence between Europe and Adria. The high-pressure Zermatt-Saas zone (Southern Switzerland) is a sequence of Mesozoic Tethys oceanic crust, which was subducted during early Alpine convergence. Peak P-T conditions for meta-AOC in the Pfulwe area and metasediments from the Trockener Steg area reached metamorphic conditions of 2.3 ± 0.2 GPa and 580 ± 30 °C (Angiboust et al., 2009). Samples PF18-25a and PF18-25c derive from a texturally preserved meta-pillow (PF18-25a: pillow core; PF18-25c: altered pillow rim) even though it experienced eclogite-facies metamorphism (Supplementary Fig. A1a). Samples PF18-20 (glaucophane-chloritoid eclogite; weakly altered AOC) and PF18-26 (chlorite-glaucophane-talc eclogite; strongly altered AOC) complete the metabasalt collection (Supplementary Fig. A1b). Further to the south, there is a small slice of the Saas-Zermatt unit with higher metamorphic conditions, the ultra-high pressure Lago di Cignana unit (Northern Italy). It comprises eclogites that derive from altered basalts, minor metagabbros and a sedimentary cover with metapelites, calcschists and quartzites that locally contain Mn-rich layers. Peak metamorphic conditions were 2.8–3.2 GPa and 600–620 °C (Groppo et al., 2009; Reinecke, 1991). The Schistes Lustrés complex (Alpine Corsica, France) represents the Ligurian part of the Jurassic western Tethys with metaophiolites and their metasedimentary cover rocks including turbidites. Peak conditions reached 2.3 ± 0.1 GPa and 520 ± 20 °C (Vitale-Brovarone et al., 2011).

Fig. 2 shows the compiled P-T conditions of the analyzed samples with respect to selected slab geotherms from Syracuse et al. (2010). The mineralogy of all samples is given in Table 1. Most high-pressure assemblages contain rutile as an accessory phase. The Mn-rich pelagic metapelites from Lago di Cignana lie on the P-T path of the Tongan slab and are potentially suited to comprise a subducted analogue of Mn-rich deep-sea sediments from DSDP site 595/596. Metasediments from Zermatt-Saas zone and Corsica give additional insights into Mo mobility and isotope fractionation at lower subduction depths. Additionally, mafic eclogites from Zermatt-Saas zone subducted to some 80 km depth complement previously measured eclogites that experienced lower pressures (Chen et al., 2019). All samples provide evidence for the mineralogy and composition of typical subducted oceanic crust just before the subarc depth is reached.

3. Analytical methods

3.1. Bulk rock major oxide and trace element analysis

3.1.1. Tongan arc lavas, sediments and oceanic crust (DSDP site 595/596)

Major and trace element investigations (preparations and measurements) of Tongan arc lavas, sediments and oceanic crust obtained from DSDP site 595/596 were performed at the Isotope Geochemistry laboratory, University of Tübingen. For major oxide composition determinations, fused beads were prepared using 1.5 g of dried and homogenized sample powder mixed with 7.5 g MERCK Spectromelt A12. Melting was conducted using an Oxiflux system from CBR analytical service reaching up to 1200 °C. Major oxide analyses were conducted using a Bruker AXS S4 Pioneer XRF device (Rh-tube at 4 kW) with 32 standardized samples. Analytical error and detection limits vary between elements and depend on sample composition. The composition of internal standards used here are compared to those of Govindaraju (1989). Absolute uncertainties are <0.250% for SiO_2 and Al_2O_3, <0.066% for TiO_2, Na_2O, MgO, MnO, CaO, and Fe_2O_3, while those for P_2O_5 are <0.009%.

For trace element analyses, the procedure as described in detail in Albut et al. (2018) was followed. In brief, ca. 30 mg of homogenized sample powders were digested either in bombs (arc lavas), or screw-top Savillex™ beakers (pelagic clays and AOC from the DSDP site 595/596) with single distilled HF-HNO3 (3:1) mix in a total volume of 3 ml acid for 3 days at 100 °C, accompanied by daily ultrasonication. After gentle evaporation at 90 °C, the samples were again dissolved in 3.5 ml 6 M HCl and cooked for two more days at 120 °C to allow disintegration of fluorides until a particle free solution was obtained. Finally, the digested sample was converted 2 times to nitrates using 3 M HNO_3 followed by gentle evaporation. In preparation for analyses, all sample unknowns were gravimetrically dissolved in 2% HNO_3 stock solutions with an aimed dilution factor of 1 k. The final measurement dilution consisted of ~1 g from that stock solution and ~ 9 g of an internal standard solution as detailed below, to yield a sample dilution factor of ~10 k. Measurements were conducted via solution quadrupole ICP-MS using a ThermoFisher Scientific iCap-Qc and following the protocols described by Eggins et al. (1997) with slight modifications after Albut et al. (2018). Main steps include the addition of an internal standard (solution enriched in ^{6}Li, In, Re and Bi) to all sample unknowns and rock reference materials which cover the full mass-range of analyzed elements. This artificial enrichment is used for instrumental mass-drift correction. Three different dilutions (10 k, 20 k, and 40 k) of the USGS W-2a reference material were used for calibration. Dimer, oxide/hydroxide interferences were corrected after Ulrich et al. (2010). To account for potential drift over the course of an entire measurement, an in-house prepared monitoring solution, consisting of digested and diluted AGV-2 and W-2a rock reference materials, was measured six times interleaved between sample unknowns. Certified rock reference materials BIR-1a and BHVO-2 prepared in the same manner as sample unknowns were used as external quality controls. Measurement precision assessed by single relative standard deviations (RSD) of the mean of multiple measurements were typically <2%. Measurement accuracy was assessed by comparing the obtained element concentrations discussed in this study with the values of Babechuk et al. (2009) as presented in Electronic Supplement ES_A. Obtained concentrations for Co, Ni, Cu, Ce, Ba, La, Sm, of BHVO-2, BIR-1a and W-2a match those of Babechuk et al. (2009) within uncertainties <2% (RSD). Slightly inferior reproducibilities (1–15% RSD) were obtained for Cs, Pb, Sb and Th and 1–32% for As. The poorer reproducibilities for Sb and As can be attributed to either very low concentration or known heterogeneity for this generation of USGS reference materials (e.g., Weis et al., 2006).

3.1.2. Metamorphic rocks

Metasediment and eclogite samples were cut with a metal saw and polished with a diamond grinding wheel to eliminate contamination from the metal saw. Further crushing was performed with a hydraulic press, which was covered with aramid fabric to protect sample against contamination. After using an agate planetary ball mill to obtain homogenized sample powder, a powder aliquot was further wet-milled again in agate, dried, and pressed to powder pellets for bulk-rock LA-ICP-MS analysis following analytical protocols presented in Peters and Pettke (2017) and Garbe-Schönberg and Müller (2014). For major and trace element analysis a GeoLas-Pro 193 nm ArF Excimer laser system (Lambda Physik) combined with an Elan DRC-e quadrupole mass spectrometer (Perkin Elmer) was used, located at the Institute of Geological Sciences, University of Bern. Optimization of the instrument was performed following previously published protocols (Peters and Pettke, 2017; Pettke et al., 2012), using GSD-1G as the external standard. Measurements of control standard OKUM Komatiite (International Association of Geoanalysts) monitored measurement quality and reproducibility.

Before measurement, the sample spot was ablated with a diameter of 160 μm to remove surface contamination (pre-ablation). The laser was set to a pulse frequency of 8 Hz and 8 J/cm^2 energy density on the sample surface with a 120 μm diameter. In total, 6 spots per sample were measured and the average was taken for the sample element concentrations (with 1 SD uncertainty on external reproducibility; Electronic Supplement ES_A). Data reduction was done using the open software SILLS (Guillong et al., 2008), with rigorous limits of detection calculation (Pettke et al., 2012).

3.2. Molybdenum purification and isotope analysis

Homogenized powder aliquots equivalent to 25–100 ng Mo (depending on Mo concentration of sample) were spiked with a purified ^{97}Mo-^{100}Mo double isotope tracer solution (Mo proportion of 1:1 spike to sample ratio). All spiked samples were then digested in a single-distilled concentrated HF-HNO_3 mixture (3:1) and re-dissolved in 6 M HCl for several days. The latter step was usually repeated to minimize the amount of fluorides. Remaining graphite in metasediment samples was physically removed by centrifuging before chemical separation. Chemical separation of Mo was achieved by applying anion- and cation-exchange chromatography following the steps reported by Wille et al. (2013). Ultimately, all samples were dissolved in 0.5 M HNO_3 for analyses conducted at the Institute of Geological Sciences, University of Bern using a ThermoFisher Scientific NeptunePlus MC-ICP-MS in low resolution mode. Sample-introduction was facilitated by a Cetac ARIDUS II desolvating nebulizer with an uptake rate of 140 - 200 μl·min^{-1}. Signals of 6 Mo isotopes (^{94}Mo$^+$, ^{95}Mo$^+$, ^{96}Mo$^+$, ^{97}Mo$^+$, ^{98}Mo$^+$ and ^{100}Mo$^+$) were measured simultaneously with interference monitors on ^{99}Ru$^+$ and ^{101}Ru$^+$ to allow correction of ^{98}Ru$^+$ on ^{98}Mo$^+$ and ^{100}Ru$^+$ on ^{100}Mo$^+$. Resistors of $10^{11}\Omega$ were used to analyze the signals of all isotopes except ^{101}Ru, which was measured using a $10^{12}\Omega$ resistor. Interference corrected $\delta^{98/95}$Mo values based on ^{99}Ru$^+$ and ^{101}Ru$^+$ correction were compared and discarded if differences were too large (>0.03‰). Background correction was applied by averaging background intensities on pure 0.5 M HNO_3 carrier solution that was measured on-peak before and after every sample analysis. Background and sample measurement consisted of 30 and 80 cycles, respectively, with a signal integration time of 4.194 s for each cycle. Our double spike correction method is based on an iterative calculation procedure reported previously (Siebert et al., 2001). Procedural blanks were generally <0.7 ng Mo. Molybdenum isotope ratios are reported as parts per thousand deviation of ^{98}Mo/^{95}Mo of the sample relative to NIST SRM 3134 (Goldberg et al., 2013; Greber et al., 2012) with an interference correction based on ^{99}Ru$^+$. Repeated measurements of the in-house J&M standard solution lot 602332B (Siebert et al., 2001) gave an isotopic difference of 0.271 ± 0.032‰ $\delta^{98/95}$Mo (2SD, $n = 56$) relative to NIST SRM 3134 (Goldberg et al., 2013), in agreement with Greber et al. (2012). Analyses of the individually digested AGV-2, BHVO-2 and W-2a whole-rock reference materials yielded a $\delta^{98/95}$Mo of −0.19 ± 0.04‰ (2SD, $n = 6$), −0.08 ± 0.05‰ (2SD, $n = 7$) and − 0.06 ± 0.04‰ (2SD, n = 6), within uncertainty to that determined by Willbold et al. (2016), Burkhardt et al. (2014), and Zhao et al. (2016). Analyses of NOD-A-1 and NOD-P-1 Mn-nodule reference materials (same digested aliquot but individual chemical separation runs) yielded a $\delta^{98/95}$Mo of −0.63 ± 0.05‰ (2SD, $n = 2$) and −0.87 ± 0.02‰ (2SD, $n = 3$), within uncertainty to that determined by Asael et al. (2013). Individual measurements of geological reference materials can be found in Electronic Supplement ES_A. We consider ±0.05‰ the long-term 2 SD reproducibility of the sample measurements as determined by the measurements of BHVO-2. This is a conservative estimate, as heterogeneity has been reported for Mo isotope ratios and overall concentration in BHVO-2 (e.g., Burkhardt et al., 2014; Willbold et al., 2016). Accurate Mo concentrations were obtained by means of inverse isotope dilution method from the double spike deconvolution (Table 2).

4. Results

Major to trace element, and Mo isotope data of analyzed samples are presented in Table 2 and Electronic Supplement ES_B. Molybdenum isotope ratios were averaged for data presentation and interpretation for samples that were analyzed multiple times.

4.1. Sediments and oceanic crust

Pelagic sediments are enriched in Mo (4–103 μg·g^{-1}) compared to average upper continental crust (UCC) Mo concentration of 1.1 μg·g^{-1} (Table 2; Rudnick and Gao, 2014). Selected trace elements like Mo, Co, Ni, and Cu, which typically show an enrichment from seawater by adsorption onto Fe-Mn-oxides (Hein et al., 2003) are highly enriched in these pelagic sediments. This is indicated by higher SCo-1 normalized Mo/Ti (19–84), Co/Ti (8–39), Ni/Ti (3–35), and Cu/Ti (6–50) ratios (Fig. 3). This reference material is a geochemically well-characterized fine-grained silty marine shale with minor input of authigenic phases from seawater. Normalization by SCo-1 and aqueous immobile Ti thus enables identification of authigenic element enrichment in investigated (meta)sediments (see Electronic Supplement ES_B for SCo-1 values used for normalization). Molybdenum concentration shows a moderate covariation with MnO (Fig. 4a) and a vertical trend in the sedimentary column starting with high concentrations in the top pelagic clays (up to 103 μg·g^{-1}) and decreasing towards the bottom porcellanite-rich layers (down to 4.0 μg·g^{-1}). Molybdenum isotope compositions show significant variations along the sediment sequence with lightest values observed at the near surface samples (down to −0.47‰) and heaviest isotopic compositions for porcellanite and chert bearing clays (up to 0.19‰; Table 2). These trends are most pronounced by comparing the Mo/Mn ratio with stratigraphic depth and $\delta^{98/95}$Mo (Fig. 4b, c). Variably altered basalts (AOC) extracted from 70 to 119 m below seafloor (mbsf) at this site have Mo concentrations of 0.15–0.51 μg·g^{-1} (Table 2) that are mostly lower than average MORB (0.46 μg·g^{-1}; Gale et al., 2013). These samples are less variable in Mo isotopic composition, ranging from −0.69‰ to −0.27‰ being lighter than MORB (−0.24 to −0.16‰, excluding the three heaviest MORB samples; Bezard et al., 2016) and AOC from ODP site 801 (−0.12 to 0.86‰; Freymuth et al., 2015; Fig. 5).

4.2. Metamorphic rocks

SiO_2, Al_2O_3, and TiO_2 as well as HFSE and REE in AOC-type eclogites do not show a large deviation from average MORB composition. Alkali and earth alkali elements as well as LILE, however, show a much larger variability due to combined effects of seafloor alteration and metamorphic modification (Supplementary Fig. A2). Molybdenum concentrations (0.038 to 0.29 μg·g^{-1}) and Mo/Ce ratios (0.0008 to 0.011) are lower compared to average MORB (Mo = 0.46 μg·g^{-1}, Mo/Ce = 0.031; Gale et al., 2013) and lower $\delta^{98/95}$Mo (−0.74 to −1.01‰) are observed compared to MORB (Fig. 5b; Table 2).

Metasediments are divided into a) pelagic metapelites: C13a, C13b, C11, COS3 and COS2 and b) clastic metasediments: Z16TB31a, Z16TB31b, Z18TB20 and COS7 (Table 1) based on the following major and trace element systematics. Major element concentrations of clastic metasedimentary rocks from the Zermatt-Saas zone and Alpine Corsica are close to that of SCo-1, while pelagic metasediments from Lago di Cignana and Alpine Corsica are enriched in MnO compared to SCo-1 (Supplementary Fig. A3). Pelagic metasediments show high SiO_2 (from 76.8 to 84.7 wt%) and lower TiO_2 and Al_2O_3 contents compared to SCo-1. All metasediments display lower Mo concentrations and Mo/Ti ratios than SCo-1 (Fig. 3). Higher SCo-1 normalized Co/Ti, Ni/Ti, and Cu/Ti ratios of 5–28, 2–7 and 2–27 are observed in pelagic metasediments compared to clastic metasediments with ratios of 1–2, 1–2, and 1–4, respectively (Fig. 3). For these elements, pelagic metasediments are similarly enriched compared to non-subducted pelagic sediments from DSDP 595/596 (Fig. 3). Furthermore, Mo negatively covaries with MnO in analyzed metasediments displaying a contrasting behavior to non-subducted pelagic sediments (Fig. 4a) indicating a decoupling of these elements during subduction. In addition, metasediments exhibit anomalously low $\delta^{98/95}$Mo ratios (down to −1.50‰; Table 2).

Table 2
Molybdenum concentrations and isotope ratios together with selected element concentrations and ratios of studied samples. 2SE = 2σ standard error.

Sample	Type	$\delta^{98/95}$Mo(‰)	2 SE	Mo (μg/g)	SiO_2 (wt%)	MgO (wt%)	Ce (μg/g)	Mo/Ce	Ba/Th
DSDP site 595/596									
595A_1	Pelagic clay	−0.470	0.018	42.0	44.3	2.74	75.2	0.559	–
595A_2A	Pelagic clay	−0.330	0.021	44.8	39.3	2.60	83.4	0.538	–
595A_3	Pelagic clay	−0.091	0.017	55.9	42.5	2.04	70.6	0.791	–
595A_4	Pelagic clay	−0.219	0.019	103	36.4	2.91	408	0.253	–
595A_5	Pelagic clay	−0.274	0.016	97.1	37.8	3.12	582	0.167	–
595A_6	Pelagic clay	−0.164	0.016	69.6	38.7	2.82	507	0.137	–
595A_7	Pelagic clay	0.161	0.016	55.7	44.9	3.00	336	0.166	–
595A_8	Pelagic clay	−0.053	0.016	34.5	43.3	3.10	300	0.115	–
595A_9	Pelagic clay	−0.030	0.014	38.7	44.9	3.15	309	0.125	–
595A_10	Pelagic clay	−0.107	0.015	31.0	45.4	3.25	278	0.112	–
595A_11	Porcellanite-rich pelagic clay	0.014	0.016	7.36	82.4	1.05	40.4	0.182	–
595A_12	Porcellanite-rich pelagic clay	0.033	0.020	6.31	69.3	1.18	41.5	0.152	–
595A_13	Porcellanite-rich pelagic clay	0.192	0.015	4.00	83.9	0.694	22.9	0.175	–
595A_16	Porcellanite-rich pelagic clay	0.072	0.018	7.11	76.0	1.18	64.6	0.110	–
595A_18	Altered basalt	−0.685	0.020	0.186	–	5.76	9.41	0.020	–
595A_19	Altered basalt	−0.494	0.016	0.154	–	6.16	9.22	0.017	–
595B_21	Altered basalt	−0.316	0.015	0.515	–	5.53	17.7	0.029	–
595B_21	Altered basalt	−0.381	0.016						
595A_23	Altered basalt	−0.278	0.013	0.352	–	–	17.1	0.021	–
595A_23	Altered basalt	−0.257	0.017						
595A_24	Altered basalt	−0.691	0.017	0.217	–	5.16	17.2	0.013	–
595B_25	Altered basalt	−0.571	0.014	0.327	–	–	18.1	0.018	–
595B_25	Altered basalt	−0.565	0.016						
595B_28	Altered basalt	−0.657	0.019	0.298	–	–	18.7	0.016	–
595B_28	Altered basalt	−0.577	0.012						
595B_31	Altered basalt	−0.597	0.015	0.187	–	–	17.6	0.011	–
595B_34	Altered basalt	−0.314	0.016	0.316	–	4.55	19.9	0.016	–
595B_37	Altered basalt	−0.432	0.015	0.161	–	6.09	12.0	0.013	–
595B_37	Altered basalt	−0.424	0.017						
Pfulwe, Zermatt									
PF18-20	AOC-type eclogite	−0.742	0.019	0.148	53.2	11.5	13.7	0.011	–
PF18-26	AOC-type eclogite	−0.825	0.014	0.293	40.1	15.8	26.9	0.011	–
PF18-25a	AOC-type eclogite	−0.919	0.018	0.0382	53.7	4.17	46.3	0.0008	–
PF18-25c	AOC-type eclogite	−1.012	0.017	0.161	46.6	0.776	51.7	0.003	–
Trockener Steg, Zermatt									
Z16TB31a	Grt-schist (clastic metasediment)	−0.149	0.014	0.635	66.7	1.79	99.7	0.006	–
Z16TB31b	Grt-schist (clastic metasediment)	−0.142	0.014	0.735	67.8	1.61	115	0.006	–
Z18TB20	Grt-schist (clastic metasediment)	−0.634	0.017	0.970	55.5	3.04	50.1	0.019	–
Lago di Cignana									
C13a	Mn-rich pelagic metasediment	−1.456	0.017	0.393	76.6	1.33	32.2	0.012	–
C13b	Mn-rich pelagic metasediment	−0.256	0.021	0.0288	78.8	1.97	41.1	0.0007	–
C11	Mn-rich pelagic metasediment	−1.500	0.018	0.0768	84.7	1.20	27.5	0.003	–
Schistes Lustrés Complex, Corsica									
COS3	Mn-rich pelagic metasediment	−0.546	0.024	0.0145	83.6	1.06	30.8	0.0005	–
COS2	Mn-rich pelagic metasediment	−0.612	0.015	0.0609	81.5	1.33	36.4	0.002	–
COS7	Clastic metasediment	−0.445	0.019	0.105	62.5	2.64	75.4	0.001	–
Ata, Tonga									
T28A1	Basalt	−0.099	0.013	0.672	50.5	7.18	6.33	0.106	349
T28A1	Basalt	−0.089	0.017						
T28A1	Basalt	−0.073	0.015						
T29A2	Basalt	−0.218	0.021	0.594	50.5	6.61	8.25	0.072	364
T30A3	Basaltic andesite	−0.161	0.013	0.677	52.7	4.97	7.59	0.089	495
T30A3	Basaltic andesite	−0.149	0.016						
T30A3	Basaltic andesite	−0.140	0.017						
T32A5	Basalt	−0.157	0.012	0.482	50.7	7.36	6.77	0.071	411
T32A5	Basalt	−0.160	0.017						
T33A6	Basalt	−0.183	0.017	0.750	50.3	7.20	6.81	0.110	450
T35A8-2	Basalt	−0.209	0.016	0.606	50.0	5.97	8.50	0.071	375
T36A9	Basalt	−0.213	0.021	0.711	50.0	6.49	8.42	0.084	388
T37A10	Basalt	−0.213	0.020	0.593	50.1	6.64	8.23	0.072	365
T38A11	Basalt	−0.329	0.018	0.673	50.7	6.23	8.66	0.078	395
T38A11	Basalt	−0.235	0.020						
T38A11	Basalt	−0.219	0.016						
T39A12	Basalt	−0.194	0.013	0.530	51.0	6.19	7.98	0.066	431
T39A12	Basalt	−0.192	0.016						
T39A12	Basalt	−0.260	0.015						
T40A13	Basalt	−0.195	0.015	0.606	51.0	6.13	7.99	0.076	434
T41A14	Basalt	−0.178	0.018	0.643	51.6	5.86	8.11	0.079	474
T42A15	Basalt	−0.161	0.017	0.701	51.7	5.89	8.53	0.082	416
Kao, Tonga									

(*continued on next page*)

Table 2 (*continued*)

Sample	Type	$\delta^{98/95}$Mo(‰)	2 SE	Mo (μg/g)	SiO_2 (wt%)	MgO (wt%)	Ce (μg/g)	Mo/Ce	Ba/Th
T15K1	Basaltic andesite	−0.059	0.015	1.06	53.3	5.60	5.83	0.181	621
T15K1	Basaltic andesite	−0.042	0.015						
T16K2	Basaltic andesite	−0.111	0.014	0.972	53.4	5.44	6.57	0.148	590
T16K2	Basaltic andesite	−0.081	0.018						
T17K3	Basaltic andesite	−0.112	0.013	0.971	53.5	5.46	6.47	0.150	598
T17K3	Basaltic andesite	−0.048	0.017						
T17K3	Basaltic andesite	−0.116	0.018						
Late, Tonga									
T21L2	Basaltic andesite	−0.136	0.015	0.813	53.5	4.43	4.57	0.178	648
T21L2	Basaltic andesite	−0.129	0.016						
T21L2	Basaltic andesite	−0.188	0.020						
T23L4	Basaltic andesite	−0.156	0.014	1.12	56.2	3.30	6.65	0.168	617
T23L4	Basaltic andesite	−0.114	0.021						
T25L6	Basaltic andesite	−0.155	0.014	0.817	53.5	4.41	4.58	0.178	603
T25L6	Basaltic andesite	−0.090	0.016						
T25L6	Basaltic andesite	−0.144	0.014						
T26L7	Basaltic andesite	−0.099	0.013	0.796	53.4	4.24	4.85	0.164	589
T26L7	Basaltic andesite	−0.097	0.018						
T26L7	Basaltic andesite	−0.124	0.015						
T27L8	Basaltic andesite	−0.142	0.014	1.16	56.3	3.34	6.64	0.174	630
T27L8	Basaltic andesite	−0.114	0.020						
Tofua, Tonga									
T2TF2	Basaltic andesite	−0.021	0.019	0.872	52.9	5.76	4.28	0.204	814
T2TF2	Basaltic andesite	−0.016	0.018						
T4TF4	Basaltic andesite	−0.083	0.017	1.18	55.5	4.45	5.45	0.217	835
T7TF7	Basaltic andesite	−0.105	0.015	0.957	53.6	4.76	5.11	0.187	797
T7TF7	Basaltic andesite	−0.068	0.017						
T9TF9	Basaltic andesite	−0.075	0.014	0.954	53.9	4.79	5.15	0.185	793
T9TF9	Basaltic andesite	−0.034	0.016						
T12TF12	Basaltic andesite	−0.116	0.013	1.36	53.6	4.76	5.09	0.268	821
T12TF12	Basaltic andesite	−0.044	0.016						
T14TF14	Basaltic andesite	−0.052	0.017	1.18	53.8	4.79	5.07	0.232	815

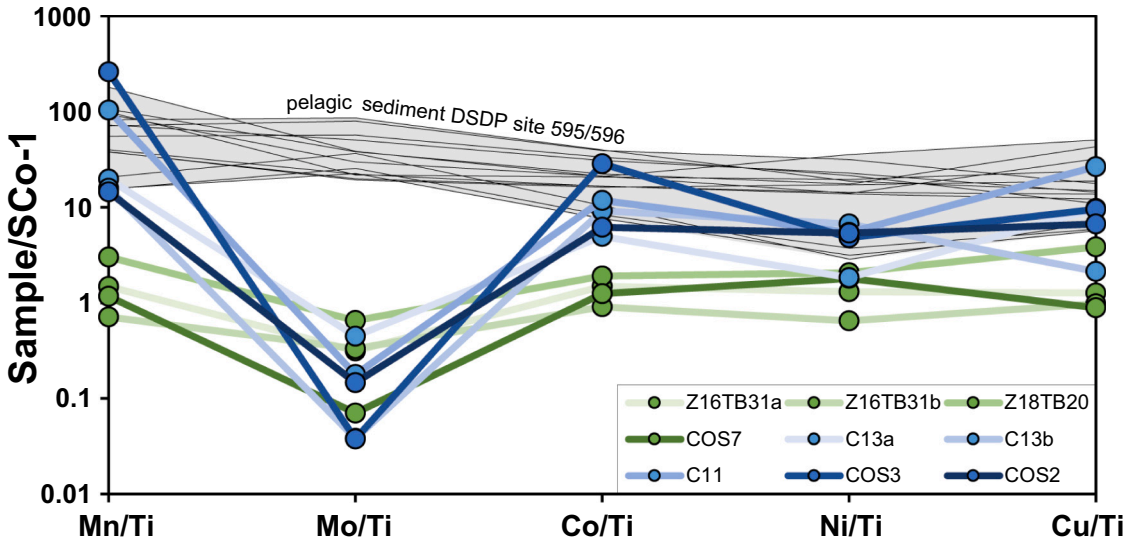

Fig. 3. Plot of reference material SCo-1 and Ti-normalized concentrations of pelagic sediments and metasediments (see Table 1 for sample types) for elements, which are commonly enriched in deep-sea Mn-oxides (Hein et al., 2003). A significant decrease in Mo/Ti is observed for metasediments compared to pelagic sediments (DSDP site 595/596). SCo-1 values are preferred values from GeoRem (Jochum et al., 2005).

4.3. Tongan arc lavas

Molybdenum concentrations within Tongan arc volcanic rocks range from 0.48 to 1.36 $\mu g \cdot g^{-1}$ (Table 2), overlapping with the average UCC Mo concentration of 1.1 $\mu g \cdot g^{-1}$ (Rudnick and Gao, 2014). The Mo isotopic range of Kao, Late, and Tofua lavas (−0.15 to −0.02‰) exceeds that of the depleted mantle (−0.20 ± 0.02‰; McCoy-West et al., 2019) and is lighter than the average upper continental crust (+0.05 to 0.15‰; Freymuth et al., 2015; Voegelin et al., 2014; Willbold and Elliott, 2017; Yang et al., 2017). Ata lavas display a larger variation (−0.26 to −0.09‰) with some samples being lighter than the depleted mantle.

The average $\delta^{98/95}$Mo of Tongan arc lavas is −0.14 ± 0.13‰ (2SD, n = 27) (Table 2). This is similar to the arc lavas from the Solomon Arc with average Mo isotopic compositions of $\delta^{98/95}$Mo = −0.10 ± 0.39‰ (2SD, n = 6; König et al., 2016). Tongan arc lavas are isotopically lighter than the wet magmatic systems of Kos (0.21 ± 0.13‰; 2SD, n = 10), the Mariana arc (without isotopically light Agrigan island; 0.06 ± 0.07‰; 2SD, n = 10), the Lesser Antilles (0.00 ± 0.26‰; 2SD, n = 10), the Izu

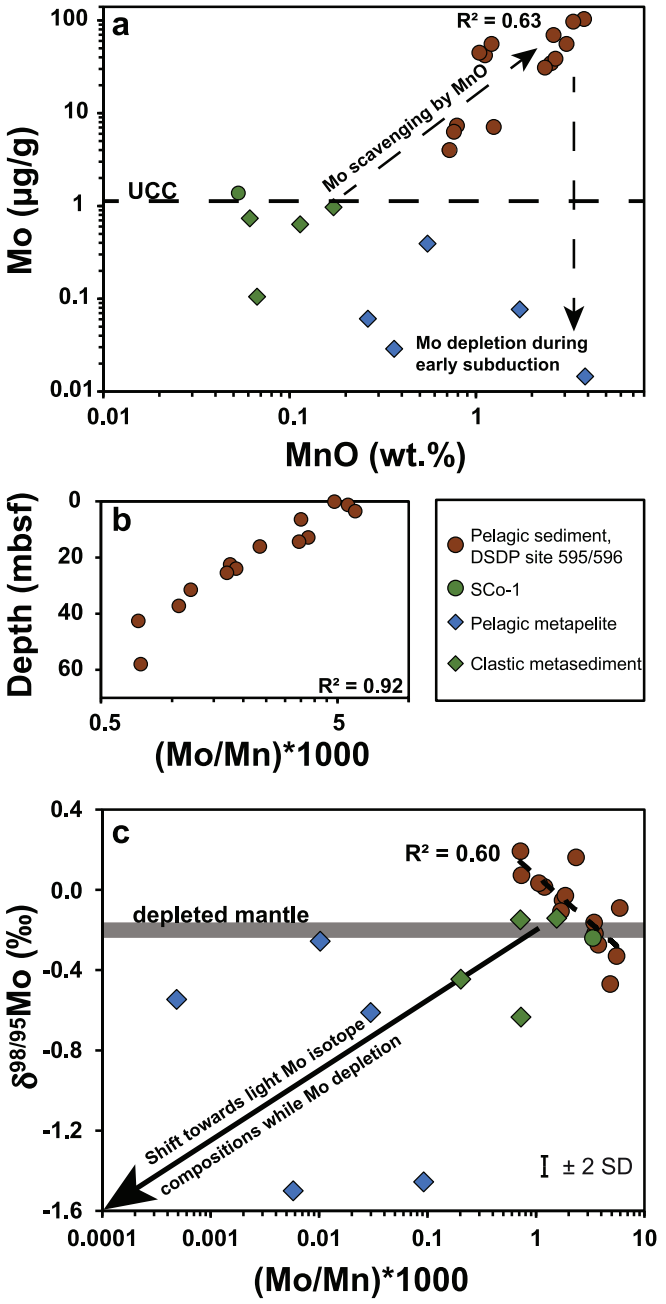

Fig. 4. Covariation plots. (a) Mo vs. MnO showing a contrasting behavior of pelagic sediments vs. metasediments and suggesting a rapid loss of Mo during the early subduction in the forearc (see text); (b) depth (m below seafloor) vs. Mo/Mn of drill core pelagic sediments and (c) $\delta^{98/95}$Mo vs. Mo/Mn of analyzed pelagic sediments show a diagenetic effect causing Mo loss and isotope fractionation towards heavier Mo, while early subduction overprint lowers $\delta^{98/95}$Mo and Mo/Mn in metasediments (see text). Depleted mantle value from McCoy-West et al. (2019). UCC value from Rudnick and Gao (2014). SCo-1 values are preferred values from GeoRem (Jochum et al., 2005). 2 SD = Long-term reproducibility (2 standard deviation).

arc (−0.03 ± 0.16‰; 2SD, n = 16) and Banda arc (without isotopically light Serua island and one sample from Teon island; 0.11 ± 0.16‰; 2SD, n = 21) (Freymuth et al., 2016; Freymuth et al., 2015; Villalobos-Orchard et al., 2020; Voegelin et al., 2014; Wille et al., 2018). Tongan arc lavas are isotopically heavier compared to Cyprus (−0.26 ± 0.26‰; 2SD, n = 7), Papua New Guinea (−0.45 ± 0.97‰; 2SD, n = 8) and young Martinique arc lavas (−0.34 ± 0.45‰; 2SD, n = 10) with moderate to significant subducted sediment components (Gaschnig et al., 2017; König et al., 2016).

SiO_2 and MgO contents within Tongan arc lavas range from 50.0 to 56.3 wt% and 7.36 to 3.30 wt%, respectively, and show moderate covariation with Mo concentration and Mo/Ce, while there is no covariation with $\delta^{98/95}$Mo (Fig. 6; SiO_2 not shown). Compared to the depleted mantle, analyzed arc lavas display a higher Mo/Ce ratio that strongly covaries with slab-derived fluid indices, such as Ba/Th and Pb/Ce, with highest values observed in Tofua, followed by Late and Kao, and then Ata (Fig. 7a,b). $\delta^{98/95}$Mo moderately covaries with Ba/Th in Tongan arc lavas (Fig. 7c), and negatively with La/Sm that indicates the degree of mantle depletion (Fig. 8). Furthermore, variably good covariation can be observed between $\delta^{98/95}$Mo and Mo/Ce with As/Ce, Sb/Ce, and Cs/Th in studied arc lavas (Fig. 9; Cs/Th not shown).

5. Discussion

5.1. Controls on the Mo isotopic compositions of oceanic sediments and AOC subducting at the Tongan trench (DSDP site 595/596)

Overall higher Mo/Ti ratios in all DSDP 595 sediments relative to SCo-1 and moderate covariation of Mo with MnO confirm an authigenic Mo enrichment from seawater on Mn-oxyhydroxides (Figs. 3, 4a). Furthermore, the ~70 m thin pelagic sediment section of DSDP site 595/596 hosts more Mo than 6000 m of Pacific mafic oceanic crust (cf. Freymuth et al., 2015), indicating that sediments dominate the Mo budget entering the Tongan subduction zone. Adsorption of molybdate onto Mn-oxyhydroxides is associated with isotope fractionation of −3‰ $\Delta^{98/95}Mo_{(MnO\text{-}seawater)}$ (Barling et al., 2001; Barling and Anbar, 2004; Siebert et al., 2003). Molybdenum isotopic compositions of Fe-Mn crusts indicate an isotopically homogeneous Mo oceanic reservoir of 2.1‰ $\delta^{98/95}$Mo for the last 60 Ma and likely during most of the Phanerozoic (Kendall et al., 2017; Siebert et al., 2003). Consequently, due to the abundant presence of Mn-oxides dominating the Mo sedimentary budget at DSDP site 595/596 we suggest an initial $\delta^{98/95}$Mo of circa −0.9‰ for the pelagic sediments at the sediment-water interface at the time of sediment deposition. Decreasing Mo/Mn and higher $\delta^{98/95}$Mo of sediments with core depth and depositional age (Fig. 4b,c) potentially record an additional early diagenetic process resulting in Mo loss and fractionation likely related to the aging of Mn-oxyhydroxides during sediment deposition and compaction, which causes a higher structural order and lower reactivity of the Mn-phases (Eitel et al., 2018).

Menard et al., 1987 found that alteration of the mafic oceanic crust (70–119 mbsf) of DSDP site 595/596 occurred at low temperature and oxidizing conditions corresponding to the lower temperature (well below 100 °C) oxidation stage 5 of Johnson and Hall (1978). The penetration of seawater into the basalt causes the oxidation of ferrous iron and the generation of H^+ (Seyfried et al., 1978), which subsequently increases the dissolution of primary minerals in the basalt. These minerals release Ca^{2+} and Mg^{2+}, which can lead to the formation of carbonate veins (Alt, 2003; Fisher, 1998). Carbonate veins found in AOC formed at low temperature for our study site (13–23 °C) and ODP site 801 (11–45 °C; Gillis and Coogan, 2011). As carbonate veins are associated with other alteration minerals in analyzed AOC samples, we use CaO/(CaO + MgO) to assess the degree of alteration. Lower $\delta^{98/95}$Mo values down to −0.69‰ with increasing degree of alteration are observed in analyzed AOC samples, suggesting a seafloor alteration control on the Mo isotopic signature (Fig. 5a). Likely, the formation of secondary minerals that formed during seafloor alteration preferentially adsorb isotopically light Mo from pore water. Depending on weathering kinetics, controlled by e.g. pore fluid residence time, composition and temperature, the pore fluid Mo reservoir is likely a variable mixture of isotopically heavy Mo derived from seawater and Mo derived from basalt weathering. Lower Mo/Ce ratios in our AOC samples indicate a net loss of Mo from MORB during alteration with rate of Mo incorporation during secondary mineral formation unable to counter-balance the Mo loss. We propose that the preferential incorporation of

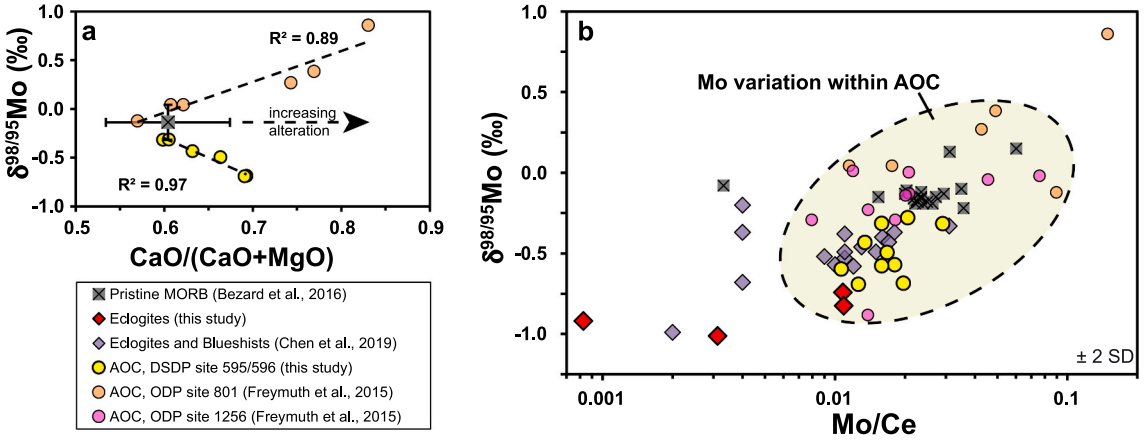

Fig. 5. Plots of (a) $\delta^{98/95}$Mo vs. CaO/(CaO + MgO) showing contrasting behaviors of Mo isotope fractionation during seafloor basalt alteration (see text). CaO and MgO contents of AOC from OPD site 801 are from Kelley et al. (2003). Error bars of average MORB indicate 2 standard deviation of the dataset from Bezard et al. (2016). 2SD reproducibility is smaller than the point size; (b) $\delta^{98/95}$Mo vs. Mo/Ce of analyzed eclogites and AOC compared with previously published data. Note the large overall variation in Mo/Ce and $\delta^{98/95}$Mo of AOC (excluding one isotopically heavy outlier of Freymuth et al. (2015)), which partly overlaps with eclogites. However, even lower Mo/Ce and $\delta^{98/95}$Mo in eclogites can be explained by Mo loss and rutile formation during subduction metamorphism (see text). 2 SD = Long-term reproducibility (2 standard deviation).

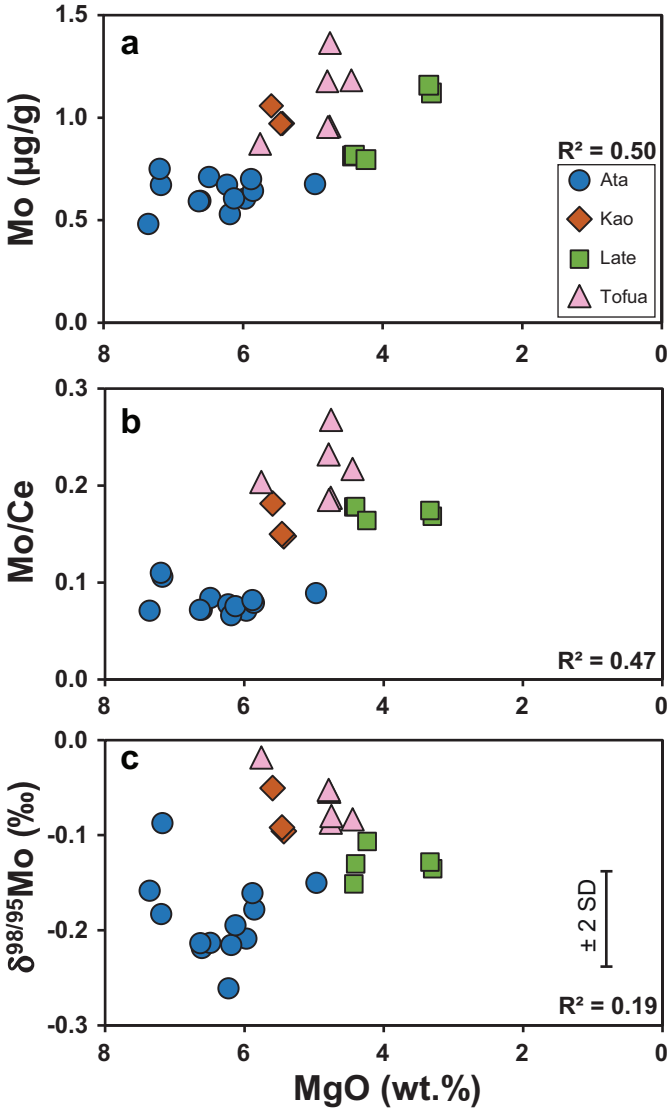

Fig. 6. Mo concentration, Mo/Ce and $\delta^{98/95}$Mo of Tongan arc lavas as a function of MgO. 2 SD = Long-term reproducibility (2 standard deviation).

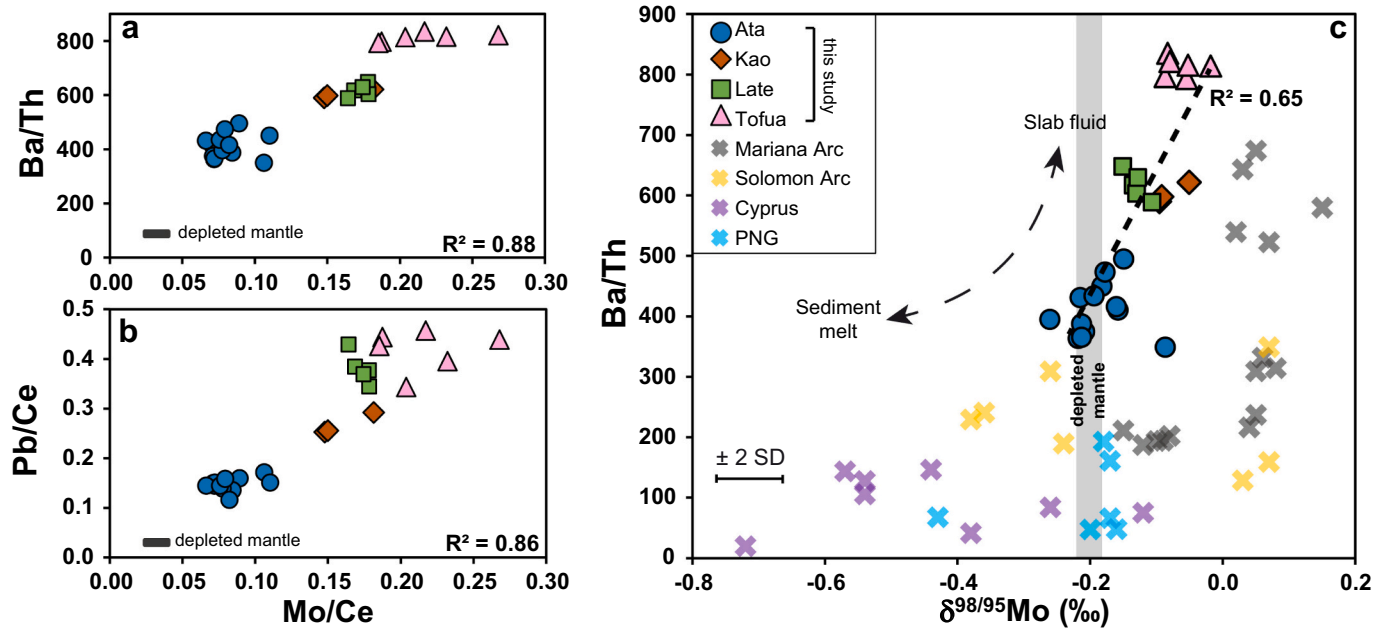

Fig. 7. Plots of: (a) Ba/Th vs. Mo/Ce and (b) Pb/Ce vs. Mo/Ce of studied arc lavas show increasing relative fluid amounts between Ata and central Tongan volcanoes with accompanied increasing Mo/Ce; (c) Ba/Th vs. $\delta^{98/95}$Mo of studied arc lavas being in line with the global trend (Freymuth et al., 2015; König et al., 2016). Depleted mantle values from Salters and Stracke (2004) and McCoy-West et al. (2019). 2 SD = Long-term reproducibility (2 standard deviation).

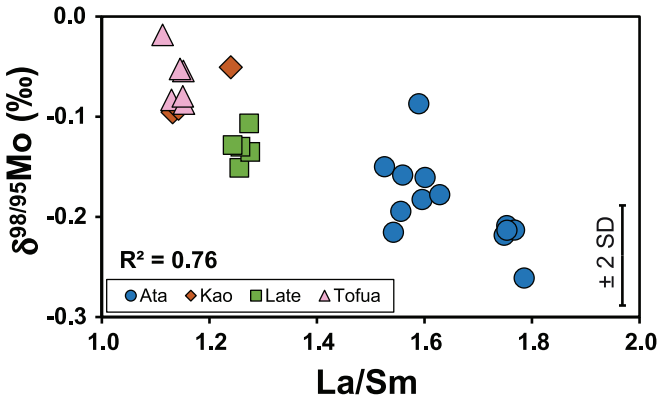

Fig. 8. Covariation diagram of $\delta^{98/95}$Mo vs. La/Sm of analyzed arc lavas shows heavier isotope signatures with increased relative mantle depletions. 2 SD = Long-term reproducibility (2 standard deviation).

isotopically light Mo in this scenario is leading to isotopically lighter Mo values compared to unaltered MORB. On the other hand, higher Mo/Ce values therefore indicate a net gain of Mo during MORB alteration which is likely seawater derived, isotopically heavy Mo. The latter scenario is observed for AOC samples from ODP site 801 (subducting at the Mariana trench), which show heavier Mo isotope signatures and higher Mo/Ce ratios with increasing seafloor alteration (Freymuth et al., 2015; Fig. 5a, b). This implies that Mo enrichment and depletion during MORB alteration can lead to heavier and lighter $\delta^{98/95}$Mo compared to the depleted mantle, respectively. Thus, different reaction kinetics might play a role on the Mo concentration and isotopic signature during seafloor alteration, producing isotopically more heterogeneous AOC than previously anticipated. This shows that the respective subduction input likely provides a unique context for each arc system and may critically complement the investigation of the subduction output (in arc lavas).

5.2. Controls on the Mo isotopic compositions of subducted oceanic crust and sediments

Clastic metasediments and, to a greater extent, pelagic metasediments have experienced a significant loss of (isotopically heavy) Mo well before entering the subarc region (Figs. 3, 4a, c). Molybdenum bound to Mn-oxide is easily mobilized, which can be already seen during early sediment deposition and diagenesis (Fig. 4b, c). The significant Mo loss in the metapelites compared to the non-subducted sediment samples from DSDP site 595/596 indicates a high mobility of Mo during early subduction especially when associated to oxyhydroxide phases. Relative to the MnO content, the metasediments are Mo depleted and retain low $\delta^{98/95}$Mo (Fig. 4c). Metapelites from Lago di Cignana represent the deepest subducted rocks of our sample set and exhibit the lightest Mo isotopic values. However, Lago di Cignana sample C13b shows higher $\delta^{98/95}$Mo in the range to that of the Corsica samples, which have experienced lower peak-pressures. Rather, the observed Mo systematics in metasediments are governed by their respective mineralogy (i.e. clastic vs. pelagic metasediments) before reaching peak P-T conditions. It may be concluded that significant Mo loss and isotope fractionation towards low $\delta^{98/95}$Mo in metasediments and especially in Mn-rich metapelites occurs already in the forearc. Therefore, it is likely that the significance of pelagic sedimentary Mo budget in subarc regions is relatively small. Fluids effervescing from mud volcanoes at the Mariana forearc show high Mo concentrations (up to ~0.6 $\mu g \cdot g^{-1}$) together with elevated Mn concentrations (Hulme et al., 2010). The authors have argued that microbially mediated changing redox conditions within the subducted sediments lead to the dissolution of metalliferous oxyhydroxides and to the mobilization of Mo during early subduction down to depth of 25 km below seafloor with estimated temperatures exceeding 200 °C (Hulme et al., 2010). The occurrence of small sulfides within the pelagic metasediments (Table 1) supports the hypothesis that sulfides formed during reducing conditions might have scavenged a small fraction of isotopically light Mo from the pore-fluid, leading to overall lighter bulk rock Mo isotopic composition (Nägler et al., 2011; Tossell, 2005). This is supported by the higher mobility of Mo compared to Co, Cu, and Ni as illustrated in lower Mo/Ti ratios relative to Co/Ti, Cu/Ti and Ni/Ti in pelagic, Mn-rich metapelites relative to their non-subducted

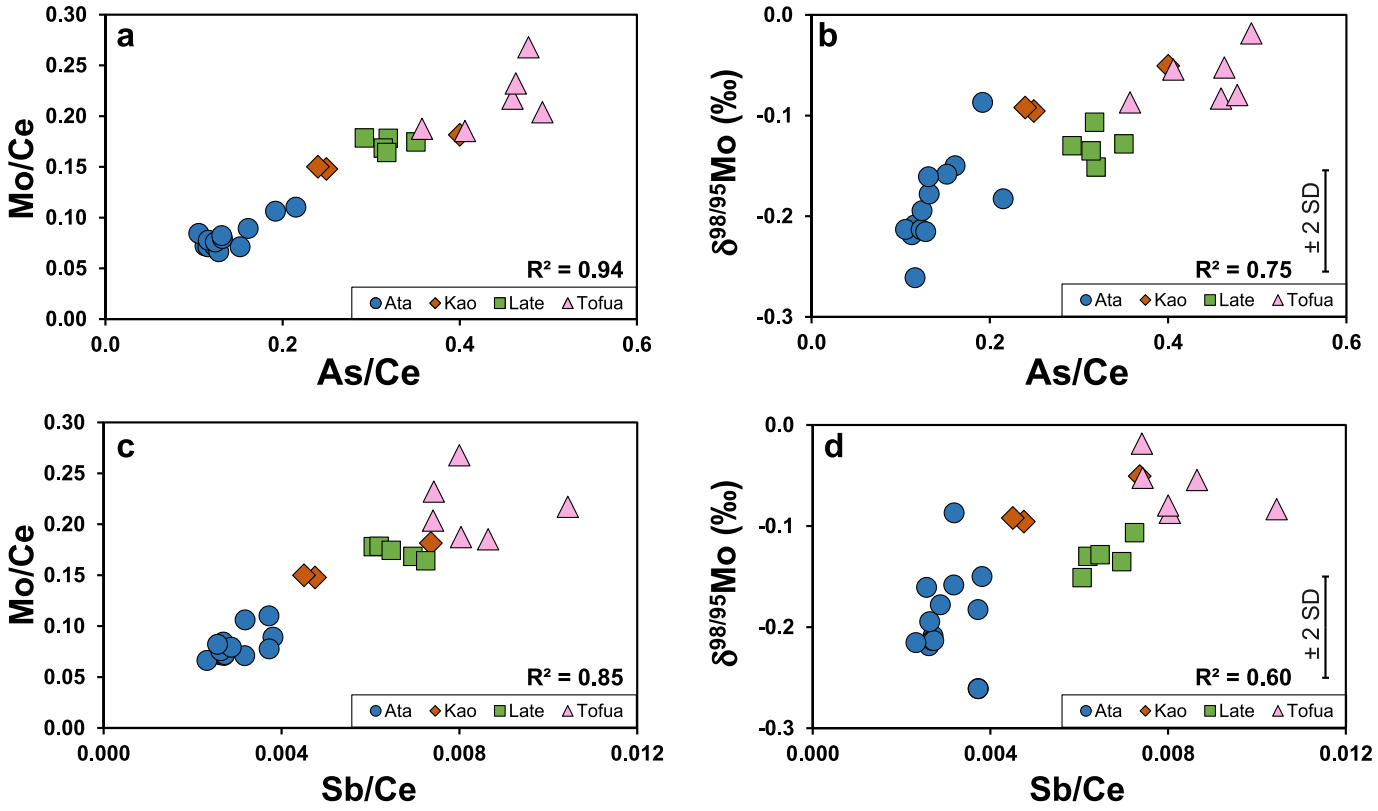

Fig. 9. Covariation plot of analyzed arc lavas with: (a) Mo/Ce vs. As/Ce; (b) $\delta^{98/95}$Mo vs. As/Ce; (c) Mo/Ce vs. Sb/Ce; (d) $\delta^{98/95}$Mo vs. Sb/Ce. 2 SD = Long-term reproducibility (2 standard deviation).

counterparts at DSDP site 595/596 (Fig. 3) and by a negative covariation between $\delta^{98/95}$Mo and chalcophile Cu of $R^2 = 0.80$ (not shown). Molybdenum concentrations in clastic metasediments tend to be less affected during early subduction, indicating that the Mo host phase has a significant effect on Mo mobility in the sedimentary pile prior to and upon early subduction.

An additional process to sulfide growth that might cause Mo isotope fractionation in metasediments is the isotopically light Mo-incorporation into metamorphic rutile. This has already been proposed for basaltic eclogites (Chen et al., 2019). The formation of rutile could be simultaneous to release of Mo from other minerals such as sulfides by pressure solution processes (Large et al., 2007). In contrast to chalcophile element systematics that are controlled by recrystallized sulfides (König et al., 2021), the preferential incorporation of Mo into rutile can therefore either inherit the bulk rock Mo budget and isotopic signature or additionally fractionate Mo isotopes during external fluid flow (Chen et al., 2019). Besides the oxygen fugacity and salinity of the subduction zone fluids, rutile dominantly controls the Mo mobility (Bali et al., 2012) and is present in most analyzed metamorphic rocks (Table 1). Due to the variable TiO_2 content in non-subducted pelagic sediments (0.05–0.9 wt%; Electronic Supplement ES_B) and generally low contents in pelagic metapelites (average 0.2 wt%; Electronic Supplement ES_B), the effect of rutile is smaller compared to mafic eclogites, which have higher modal abundances of rutile. Further Mo isotopic analyses on single sulfides and rutile of metasediments are required to quantify the different isotope fractionation processes.

In a plot of $\delta^{98/95}$Mo vs. Mo/Ce (Fig. 5b) the range defined by our AOC samples coincides with our eclogite samples PF18–20 and PF18–26 and most of the mafic eclogites and blueschist samples analyzed by Chen et al. (2019), whereas some samples herein display even lower Mo/Ce, indicating that these Mo signatures could have been dominantly influenced by seafloor alteration processes. Furthermore, these eclogites cover peak metamorphic conditions between 1.7–2.5 GPa and 550–670 °C corresponding to forearc depths (Angiboust et al., 2009; Chen et al., 2019, and references therein; Fig. 2) suggesting that in some situations a large fraction of slab-Mo is already lost before entering subarc regions. As rutile is the dominant host of Mo in mafic eclogites (Chen et al., 2019; Zack et al., 2002) with ~85% of bulk Mo for PF18-20 and PF18-26 and ~54% for PF18-25a, this implies that most of the Mo is isotopically light well before entering subarc regions. Cerium is mainly hosted in allanite/epidote that is stable during progressive subduction zone metamorphism (Hermann, 2002). Therefore, bulk Mo/Ce and Mo isotope signatures will remain unmodified from upper blueschist-facies conditions (~400 °C, 45 km depth) onwards. Consequently, the lower Mo/Ce ratios in these eclogites imply that most Mo was lost prior to rutile crystallization. However, eclogite samples PF18-25a and PF18-25c show $\delta^{98/95}$Mo down to −1.01‰ and lower Mo/Ce ratios, down to 0.0008, and are therefore outside the $\delta^{98/95}$Mo vs. Mo/Ce field defined by AOC samples investigated so far (Fig. 5b). This is line with several eclogite (and one blueschist) samples analyzed by Chen et al. (2019) and indicates a larger loss of Mo accompanied by an additional Mo isotope fractionation during subduction (Fig. 5b). Chen et al. (2019) interpreted low Mo/Ce ratios to be the result of selective mobilization of Mo relative to Ce during the interaction with fluids derived from the underlying serpentinized mantle. This does not apply for our investigated samples, as serpentine is stable in the adjacent ultramafic rocks (see also Fig. 2) and no evidence exists for a massive external fluid input. Indeed, these samples still display pristine pillow textures despite the eclogite-facies overprint (Supplementary Fig. A1), providing evidence for minimal deformation and external fluid input during subduction. Therefore, we interpret the low $\delta^{98/95}$Mo and Mo/Ce ratios in our mafic eclogites as a result of extensive seafloor alteration but do not want to exclude the potential of a superimposed Mo mobilization and fractionation process during subduction metamorphism within the forearc.

In summary, slab-released Mo, transported by aqueous fluids into the forearc mantle, may be isotopically heavy compared to residual

eclogites. Metasediments record lighter Mo isotopic compositions when compared to their respective protoliths. Before entering subarc regions, most of the remaining eclogitic Mo is isotopically light and locked in rutile.

5.3. Controls on the Mo isotopic compositions of Tongan arc lavas

Molybdenum concentrations increase with increasing SiO_2 and decreasing MgO contents (Fig. 6a; SiO_2 not shown); however, this relationship is likely not related to its incompatible behavior during fractional crystallization as indicated by increasing Mo/Ce ratios with decreasing MgO (Fig. 6b; Mo and Ce being of very similar compatibility during mantle melting). As degrees of mantle melting for studied Tongan arc islands are well above 10%, (e.g., Beier et al., 2017; Myeong et al., 2020), the observed Mo/Ce ratios cannot be explained through low-degree partial melting of 2–3% (Wang and Becker, 2018) (Fig. 6b). Also, the heavier Mo isotopic composition of Tongan arc lavas compared to depleted mantle cannot be explained by fractional crystallization of hydrous phases (Voegelin et al., 2014), since no clear relationship between indices of magmatic differentiation, such as MgO and SiO_2 concentration, and $\delta^{98/95}$Mo can be observed (Fig. 6c; SiO_2 not shown). The highest $\delta^{98/95}$Mo values are observed in arc lavas from Tofua, where volatile loss at shallow levels in the crust and temperatures above 950 °C, precludes the stabilization of amphibole (Caulfield et al., 2012). This indicates inhibited hydrous differentiation consistent with a complete absence of hydrous phases (Caulfield et al., 2012).

Elevated ratios of Ba/Th, Pb/Ce and Mo/Ce of Tongan arc lavas likely show an addition of Ba, Pb, and Mo, relative to their respective fluid-immobile denominators (Fig. 7a, b). Most pronounced fluid addition is thus seen in Tofua lavas, followed by Late and Kao. This coincides with $\delta^{98/95}$Mo ratios significantly heavier than mantle for these islands (Fig. 7c). Ata lavas on the other hand, show both lowest fluid-induced element ratios and $\delta^{98/95}$Mo that are (mostly) within uncertainty of mantle values. Overall, observed positive covariations between fluid parameters, relative Mo enrichments, and $\delta^{98/95}$Mo suggest slab-derived fluid enrichment of isotopically heavy Mo into the Tongan subarc mantle (Fig. 7). This is in agreement with results for arc lavas from the Mariana arc (Freymuth et al., 2015), Solomon Islands (König et al., 2016) and Izu arc (Villalobos-Orchard et al., 2020), where heavier Mo isotopic compositions than mantle have been linked to pronounced slab-derived aqueous fluid-enrichment. In comparison to other arc settings, arc lavas from Tofua show the highest Ba/Th ratios relative to a given $\delta^{98/95}$Mo (Fig. 7c). This is in part because slab-derived fluid effects are more notable relative to a highly depleted mantle wedge source (see also Fig. 8), as also observed based on radiogenic isotope systematics in Izu arc lavas (Villalobos-Orchard et al., 2020).

5.4. The Mo subduction recycling conundrum

There is clear evidence that the shift in Mo isotopic composition in arc lavas is related to the addition of a subduction component (Fig. 7). However, the heavy Mo isotopic signature of Tongan arc lavas is difficult to explain via a simple aqueous fluid addition from the subducted slab at subarc depth (> 100 km). Large proportions of primary Mo hosted in the subducting sediment and altered oceanic crust are likely lost to the hanging wall mantle at forearc depths. This Mo mobilization likely depends on the stability of the Mo host phases during early subduction metamorphism. Furthermore, when rutile forms in forearc regions at around 1–1.5 GPa it incorporates most of the remaining and preferentially isotopically light Mo in subducted oceanic crust and sediments well before entering subarc regions. Based on coupled Pb and Mo isotope systematics, the deep, unaltered oceanic crust has been proposed as dominant source for slab-derived Mo in Mariana arc lavas (Freymuth et al., 2015). Because the solubility of rutile is very low in common subduction zone fluids (Audétat and Keppler, 2005) and Mo is highly compatible in rutile (Bali et al., 2012), rutile-bound Mo is unavailable for incorporation into slab dehydration fluid. Consequently, slab-derived aqueous fluids released at sub arc depth can be expected to transport negligible Mo. A process to mobilize rutile-bound Mo is partial melting of subducted AOC and metasediments at subarc depth, which would then provide an isotopically light Mo slab component of arc magmas. Such a model is in line with extremely low $\delta^{98/95}$Mo observed in Cyprus basalts and boninites, which was interpreted to be the result of sediment melt contribution of isotopically fractionated material (König et al., 2016). Furthermore, the Cyprus basalts and boninites display low Mo/Ce (and Ba/Th) suggesting that the subducted material already lost Mo prior to slab melting (König et al., 2016). The light $\delta^{98/95}$Mo, down to −0.26‰, and low Mo/Ce in Ata lavas might represent a signal from sediment melts. However, a clear geochemical identification of slab derived melt input into the subarc mantle remains elusive likely due to the lower degree of mantle depletion below Ata compared to Cyprus and $\delta^{98/95}$Mo close to the depleted mantle value. Therefore, we argue that the subarc slab does not represent a simple, single-stage Mo source to account for the isotopically heavy fluid-rich signatures of Kao, Late, and Tofua arc lavas. Instead, a multi stage Mo-recycling process involving the forearc mantle is required.

5.5. A possible solution to the Mo subduction recycling conundrum for the Tongan subduction zone

Our new data from high-pressure rocks suggest that Mo mobility and isotope fractionation occurs during prograde subduction in the forearc region. The preferential incorporation of light Mo in eclogites and metasediments suggests that the Mo fluid flux infiltrating the forearc mantle wedge is isotopically heavy. This may lead to forearc serpentines with higher Mo/Ce ratios and higher $\delta^{98/95}$Mo compared to the overall Mo isotope composition of the subducted material. A potential contribution of the metasomatized forearc to subarc source regions (cf. Savov et al., 2005) of the Tongan arc islands could thus explain the observed Mo isotope systematics in Tongan arc lavas. Although forearc serpentines have not been measured for Mo concentration and isotope ratios so far, it is well known that serpentinization of the forearc mantle associated with shallow slab-derived fluid influx leads to an increase in bulk rock fluid mobile element concentrations, such as B, As, Cs, Sb and Li (e.g., Savov et al., 2007). This hypothesis can be tested by comparing $\delta^{98/95}$Mo and Mo/Ce ratios with these shallow slab-derived fluid mobile elements. Moderate to strong covariation is observed between As/Ce, Sb/Ce, and Cs/Th against $\delta^{98/95}$Mo as well as Mo/Ce (Fig. 9; Cs/Th not shown). This indicates that the isotopically heavy slab-derived fluid signature in Tongan arc lavas might be derived from the metasomatized forearc mantle. The enrichment of these elements is associated with slab-derived fluid interaction with the overlying mantle in forearc regions at 200–600 °C (e.g., Cannaò and Malaspina, 2018 and references therein), which leads to a serpentinized forearc mantle reservoir with a distinctive geochemical fingerprint (e.g., Savov et al., 2007). The incorporation of such a forearc geochemical signature into arc lavas requires more complex models of arc magma genesis.

Tonarini et al. (2011) proposed a multi-stage subduction model, where early stage fluids released during shallow metamorphic dehydration of the slab variably metasomatize the overlying mantle wedge. Subsequent basal erosion transports the hanging wall serpentinized mantle material to subarc regions, where hydrous mineral breakdown conditions are likely reached along the slab surface geotherm (Fig. 2). The model was suggested based on compositions of arc lavas from the South Sandwich Islands, subducting marine sediments and dredged frontal arc peridotites. By analogy, B isotope compositions and mass balance calculations showed that high δ^{11}B in the arc lavas can only be explained by subduction/basal erosion of the forearc mantle wedge followed by the release of previously incorporated B at higher temperatures (Tonarini et al., 2011). This alternative process is suitable to explain increasing contents of B and other fluid-mobile elements and also increasing δ^{11}B in the subarc mantle wedge (Tonarini et al., 2011).

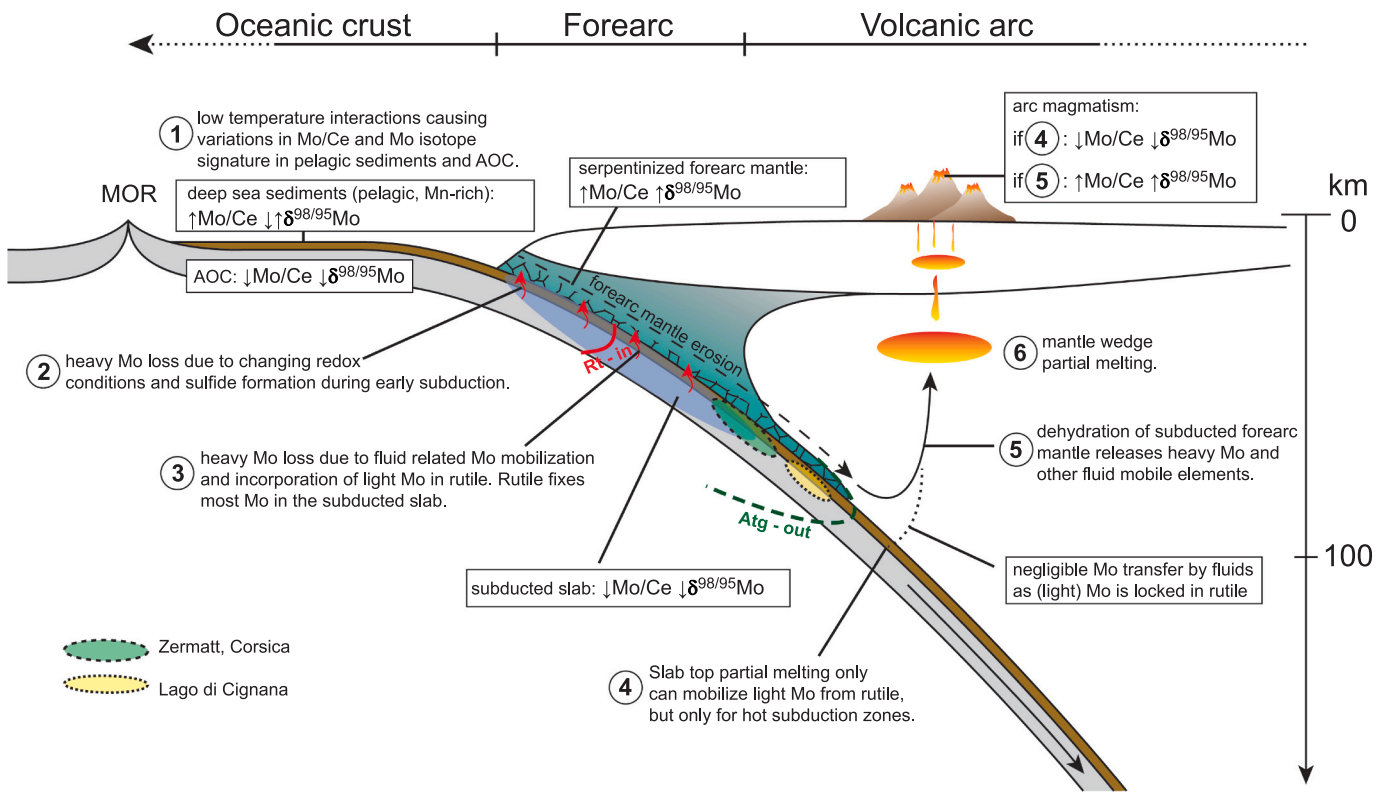

Fig. 10. Illustration of the main processes in the Tongan subduction zone and the approximate peak P-T positions of studied metamorphic rocks. Furthermore, the Mo/Ce and Mo isotope ratios (compared to mantle) of the important Mo reservoirs are shown. Dehydration and loss of heavy Mo due to isotope fractionation during secondary mineral formation (2,3) leads to serpentinization of the overlying forearc mantle and enriches it in heavy Mo. Subsequent erosion and possibly slab rollback transports enriched forearc mantle into greater depths leading to antigorite dehydration and liberation of fluids with heavy Mo (5). Due to fluid induced melting in the mantle wedge, fluid-derived Mo is finally recycled into arc magmatism.

There is thus significant reasoning that similar processes might act in the Tongan subduction zone. Geophysical data indicate serpentinization of ~30% of the Tongan forearc mantle (Contreras-Reyes et al., 2011), providing evidence for extensive interaction of the forearc mantle with slab-derived aqueous fluids. Furthermore, the absence of serpentine mud volcanoes at the Tongan trench indicates a rapid tectonic erosion of the forearc hanging wall, as the mantle is removed too quickly before being completely altered to serpentinite (Clift and Vannucchi, 2004; Contreras-Reyes et al., 2011). We therefore propose that Mo recycling at the Tongan arc might follow a similar multi-stage subduction recycling process as suggested by Tonarini et al. (2011) for the South Sandwich Islands based on B (Fig. 10). Besides simple downdrag of serpentinized portions in a compressive regime, a more complex recycling process could involve the influence of slab rollback. Indeed, the Tongan subduction zone retreated by about 1800 km during the last 90 My due to slab rollback (Schellart et al., 2006) with the development of a magmatically active back-arc basin spreading. Such a fast rollback may result in migration of the wedge asthenospheric mantle along with the retreating subduction interface to eventually reach a position beneath earlier serpentinized lithospheric mantle portions. This would lead to dehydration of serpentinites that have been previously enriched in fluid mobile elements such as Mo, As, Sb, and Cs. Partial melts derived from the hot mantle wedge may then incorporate these fluids with a heavy Mo isotope signature en route to the arc crust where magmas evolve and eventually erupt. Hence, we propose multi-stage dehydration and addition of forearc geochemical signatures to explain the Mo systematics of Tongan arc lavas. Our findings suggest that the subduction zone dynamics (accretion vs. erosion) and slab motion (rollback) has to be taken into account when investigating subduction zone recycling of Mo and other slab components to the source of arc magmas.

6. Conclusion

Based on a comparison of input to output geochemical and Mo isotope data at the Tongan subduction zone together with metamorphosed analogues of subducted oceanic crust and marine sediments we conclude:

1. Molybdenum mobility and isotope fractionation in subducting sediments are strongly dependent on the Mo host phase (Mn-oxide vs. silicate vs. rutile). Furthermore, changing redox-conditions during early subduction lead to Mn-oxide dissolution and significant Mo mobilization. These redox changes result in potential sulfide formation and incorporation of light Mo into sulfides.
2. Low temperature seawater alteration of the oceanic crust can lower Mo/Ce and shift Mo isotopic signature to smaller values and may at least partially explain Mo signatures that are then found in mafic eclogites. Our data contrast those reported for AOC at ODP site 801 (Freymuth et al., 2015), revealing that the processes of mafic oceanic crust alteration are likely diverse. Importantly, the combined data set suggests that AOC encompasses a large range in Mo concentrations and isotopic compositions, eventually available for subduction.
3. Comparison of AOC and pelagic sediment from DSDP site 595/596 with their subducted counterparts reveals significant Mo loss and isotopic fractionation already in the forearc – likely leading to higher Mo/Ce and $\delta^{98/95}$Mo in the serpentinized hanging wall mantle of the forearc. In mafic eclogites, the largest fraction of Mo is bound in rutile forming in forearc regions, thus locking this Mo at sub-solidus conditions down to subarc depths, implying negligible Mo mobilization by slab-derived fluids to the subarc mantle. At higher temperatures, this isotopically light Mo can be remobilized by partial slab melting.

4. Tongan arc lavas show higher $\delta^{98/95}$Mo than ambient mantle. Positive covariations with fluid proxies link this Mo signature to influx of isotopically heavy fluids from the slab. Such an isotopically heavy, slab-derived fluid signature is most pronounced where the highest degrees of mantle rock melt depletion occurred. Low Mo/Ce and $\delta^{98/95}$Mo in the subducted slab cannot directly explain slab-derived fluid Mo in Tongan arc lavas. The integration of the earlier metasomatized forearc mantle to subarc regions provides a suitable alternative process to explain observed variations in arc lavas by releasing previously incorporated isotopically heavy Mo. The recycling of the forearc mantle in subduction zones is supported by correlations of Mo/Ce and $\delta^{98/95}$Mo with fluid-mobile elements that are commonly enriched in the forearc mantle. This process possibly highlights that subduction erosion and slab rollback is important for Mo and possibly other element recycling in subduction zone settings.

Supplementary data to this article can be found online at https://doi.org/10.1016/j.chemgeo.2021.120231.

Declaration of Competing Interest

The authors declare that they have no known competing financial interests or personal relationships that could have appeared to influence the work reported in this paper.

Acknowledgements

This work was funded by the Swiss National Science Foundation, Switzerland (Grant 182508) to M.W. S.K. and C.R. acknowledge ERC Starting Grant 636808 to S.K. (O2RIGIN). The MC-ICP-MS at the Institute of Geological Sciences, University of Bern used in this study was acquired within the framework of the NCCR project PlanetS (Grant nr. 1NF40-141881). S.K. thanks the Tongan Geological Services for logistical support during the sampling campaign. This research used further samples provided by the International Ocean Discovery Program (IODP) to S.K. and M.W. We are grateful to Nathalie Zumbrunn, Thomas Bovay, Elias Kempf, and Diana Roos for providing samples and data from Zermatt and A. Vitale-Brovarone with assistance in fieldwork in Corsica. David Janssen is acknowledged for discussions that contributed to this manuscript. We also wish to thank Alex McCoy-West and 2 anonymous reviewers for constructive reviews, as well as Mirjam Schaller and Balz Kamber for editorial handling.

References

Albut, G., Babechuk, M.G., Kleinhanns, I.C., Benger, M., Beukes, N.J., Steinhilber, B., Smith, A.J.B., Kruger, S.J., Schoenberg, R., 2018. Modern rather than Mesoarchaean oxidative weathering responsible for the heavy stable Cr isotopic signatures of the 2.95 Ga old Ijzermijn iron formation (South Africa). Geochim. Cosmochim. Acta 228, 157–189. https://doi.org/10.1016/j.gca.2018.02.034.

Alt, J.C., 2003. Stable isotopic composition of upper oceanic crust formed at a fast spreading ridge, ODP Site 801. Geochem. Geophys. Geosyst. 4 https://doi.org/10.1029/2002GC000400 n/a-n/a.

Angiboust, S., Agard, P., Jolivet, L., Beyssac, O., 2009. The Zermatt-Saas ophiolite: the largest (60-km wide) and deepest (c. 70–80 km) continuous slice of oceanic lithosphere detached from a subduction zone? Terra Nov. 21, 171–180. https://doi.org/10.1111/j.1365-3121.2009.00870.x.

Asael, D., Tissot, F.L.H., Reinhard, C.T., Rouxel, O., Dauphas, N., Lyons, T.W., Ponzevera, E., Liorzou, C., Chéron, S., 2013. Coupled molybdenum, iron and uranium stable isotopes as oceanic paleoredox proxies during the Paleoproterozoic Shunga Event. Chem. Geol. 362, 193–210. https://doi.org/10.1016/j.chemgeo.2013.08.003.

Audétat, A., Keppler, H., 2005. Solubility of rutile in subduction zone fluids, as determined by experiments in the hydrothermal diamond anvil cell. Earth Planet. Sci. Lett. 232, 393–402. https://doi.org/10.1016/j.epsl.2005.01.028.

Babechuk, M.G., Kamber, B.S., Greig, A., Canil, D., Kodolányi, J., 2009. The behaviour of tungsten during mantle melting revisited with implications for planetary differentiation time scales. Geochim. Cosmochim. Acta 74, 1448–1470. https://doi.org/10.1016/j.gca.2009.11.018.

Bali, E., Keppler, H., Audetat, A., 2012. The mobility of W and Mo in subduction zone fluids and the Mo-W-Th-U systematics of island arc magmas. Earth Planet. Sci. Lett. 351–352, 195–207. https://doi.org/10.1016/j.epsl.2012.07.032.

Ballance, P.F., Scholl, D.W., Vallier, T.L., Stevenson, A.J., Ryan, H., Herzer, R.H., 1989. Subduction of a Late Cretaceous Seamount of the Louisville Ridge at the Tonga Trench: a model of normal and accelerated tectonic erosion. Tectonics 8, 953–962. https://doi.org/10.1029/TC008i005p00953.

Barling, J., Anbar, A.D., 2004. Molybdenum isotope fractionation during adsorption by manganese oxides. Earth Planet. Sci. Lett. 217, 315–329. https://doi.org/10.1016/S0012-821X(03)00608-3.

Barling, J., Arnold, G.L., Anbar, A.D., 2001. Natural mass-dependent variations in the isotopic composition of molybdenum. Earth Planet. Sci. Lett. 193, 447–457. https://doi.org/10.1016/S0012-821X(01)00514-3.

Beier, C., Turner, S.P., Haase, K.M., Pearce, J.A., Münker, C., Regelous, M., 2017. Trace element and isotope geochemistry of the northern and central tongan islands with an emphasis on the genesis of high Nb/Ta signatures at the northern volcanoes of Tafahi and Niuatoputapu. J. Petrol. 58, 1073–1106. https://doi.org/10.1093/petrology/egx047.

Bevis, M., Taylor, F.W., Schutz, B.E., Recy, J., Isacks, B.L., Helu, S., Singh, R., Kendrick, E., Stowell, J., Taylor, B., Calmantli, S., 1995. Geodetic observations of very rapid convergence and back-arc extension at the Tonga arc. Nature 374, 249–251. https://doi.org/10.1038/374249a0.

Bezard, R., Fischer-Gödde, M., Hamelin, C., Brennecka, G.A., Kleine, T., 2016. The effects of magmatic processes and crustal recycling on the molybdenum stable isotopic composition of Mid-Ocean Ridge Basalts. Earth Planet. Sci. Lett. 453, 171–181. https://doi.org/10.1016/j.epsl.2016.07.056.

Burkhardt, C., Hin, R.C., Kleine, T., Bourdon, B., 2014. Evidence for Mo isotope fractionation in the solar nebula and during planetary differentiation. Earth Planet. Sci. Lett. 391, 201–211. https://doi.org/10.1016/j.epsl.2014.01.037.

Cannaò, E., Malaspina, N., 2018. Oceanic to continental subduction: implications for the geochemical and redox evolution of the supra-subduction mantle. Geosphere 14, 2311–2336. https://doi.org/10.1130/GES01597.1.

Casalini, M., Avanzinelli, R., Tommasini, S., Elliott, T., Conticelli, S., 2019. Ce/Mo and molybdenum isotope systematics in subduction-related orogenic potassic magmas of Central-Southern Italy. Geochem. Geophys. Geosyst. 20, 2753–2768. https://doi.org/10.1029/2019GC008193.

Caulfield, J.T., Turner, S.P., Smith, I.E.M., Cooper, L.B., Jenner, G.A., 2012. Magma Evolution in the Primitive, Intra-oceanic Tonga Arc: Petrogenesis of Basaltic Andesites at Tofua Volcano. J. Petrol. 53, 1197–1230. https://doi.org/10.1093/petrology/egs013.

Chen, S., Hin, R.C., John, T., Brooker, R., Bryan, B., Niu, Y., Elliott, T., 2019. Molybdenum systematics of subducted crust record reactive fluid flow from underlying slab serpentine dehydration. Nat. Commun. 10 https://doi.org/10.1038/s41467-019-12696-3.

Clift, P., Vannucchi, P., 2004. Controls on tectonic accretion versus erosion in subduction zones: Implications for the origin and recycling of the continental crust. Rev. Geophys. 42 https://doi.org/10.1029/2003RG000127.

Contreras-Reyes, E., Grevemeyer, I., Watts, A.B., Flueh, E.R., Peirce, C., Moeller, S., Papenberg, C., 2011. Deep seismic structure of the Tonga subduction zone: implications for mantle hydration, tectonic erosion, and arc magmatism. J. Geophys. Res. Solid Earth 116. https://doi.org/10.1029/2011JB008434.

Eggins, S.M., Woodhead, J.D., Kinsley, L.P.J., Mortimer, G.E., Sylvester, P., McCulloch, M.T., Hergt, J.M., Handler, M.R., 1997. A simple method for the precise determination of ≥ 40 trace elements in geological samples by ICPMS using enriched isotope internal standardisation. Chem. Geol. 134, 311–326. https://doi.org/10.1016/S0009-2541(96)00100-3.

Eitel, E.M., Zhao, S., Tang, Y., Taillefert, M., 2018. Effect of manganese oxide aging and structure transformation on the kinetics of thiol oxidation. Environ. Sci. Technol. 52, 13202–13211. https://doi.org/10.1021/acs.est.8b03993.

Escrig, S., Bézos, A., Goldstein, S.L., Langmuir, C.H., Michael, P.J., 2009. Mantle source variations beneath the eastern lau spreading center and the nature of subduction components in the lau basin-tonga arc system. Geochem. Geophys. Geosyst. 10 https://doi.org/10.1029/2008GC002281.

Ewart, A., Collerson, K.D., Regelous, M., Wendt, J.I., Niu, Y., 1998. Geochemical evolution within the Tonga-Kermadec-Lau arc-back-arc systems: the role of varying mantle wedge composition in space and time. J. Petrol. Oxford Acad. https://doi.org/10.1093/PETROJ/39.3.331.

Fisher, A.T., 1998. Permeability within basaltic oceanic crust. Rev. Geophys. 36, 143–182. https://doi.org/10.1029/97RG02916.

Freymuth, H., Vils, F., Willbold, M., Taylor, R.N., Elliott, T., 2015. Molybdenum mobility and isotopic fractionation during subduction at the Mariana arc. Earth Planet. Sci. Lett. 432, 176–186. https://doi.org/10.1016/j.epsl.2015.10.006.

Freymuth, H., Elliott, T., van Soest, M., Skora, S., 2016. Tracing subducted black shales in the Lesser Antilles arc using molybdenum isotope ratios. Geology 44, 987–990. https://doi.org/10.1130/G38344.1.

Gale, A., Dalton, C.A., Langmuir, C.H., Su, Y., Schilling, J.G., 2013. The mean composition of ocean ridge basalts. Geochem. Geophys. Geosyst. 14, 489–518. https://doi.org/10.1029/2012GC004334.

Garbe-Schönberg, D., Müller, S., 2014. Nano-particulate pressed powder tablets for LA-ICP-MS. In: Journal of Analytical Atomic Spectrometry. Royal Society of Chemistry, pp. 990–1000. https://doi.org/10.1039/c4ja00007b.

Gaschnig, R.M., Reinhard, C.T., Planavsky, N.J., Wang, X., Asael, D., Chauvel, C., 2017. The molybdenum isotope system as a tracer of slab input in subduction zones: an example from Martinique, Lesser Antilles Arc. Geochem. Geophys. Geosyst. 18, 4674–4689. https://doi.org/10.1002/2017GC007085.

Gillis, K.M., Coogan, L.A., 2011. Secular variation in carbon uptake into the ocean crust. Earth Planet. Sci. Lett. 302, 385–392. https://doi.org/10.1016/j.epsl.2010.12.030.

Goldberg, T., Gordon, G., Izon, G., Archer, C., Pearce, C.R., McManus, J., Anbar, A.D., Rehkämper, M., 2013. Resolution of inter-laboratory discrepancies in Mo isotope

data: an intercalibration. J. Anal. At. Spectrom. 28, 724–735. https://doi.org/10.1039/c3ja30375f.
Gordon, G.W., Lyons, T.W., Arnold, G.L., Roe, J., Sageman, B.B., Anbar, A.D., 2009. When do black shales tell molybdenum isotope tales? Geology 37, 535–538. https://doi.org/10.1130/G25186A.1.
Govindaraju, K., 1989. 1989 Compilation of working values and sample description for 272 geostandards. Geostand. Newslett. 13, 1–113. https://doi.org/10.1111/j.1751-908X.1989.tb00476.x.
Greber, N.D., Siebert, C., Nägler, T.F., Pettke, T., 2012. δ98/95Mo values and molybdenum concentration data for NIST SRM 610, 612 and 3134: towards a common protocol for reporting Mo data. Geostand. Geoanal. Res. 36, 291–300. https://doi.org/10.1111/j.1751-908X.2012.00160.x.
Greber, N.D., Puchtel, I.S., Nägler, T.F., Mezger, K., 2015. Komatiites constrain molybdenum isotope composition of the Earth's mantle. Earth Planet. Sci. Lett. 421, 129–138. https://doi.org/10.1016/j.epsl.2015.03.051.
Groppo, C., Beltrando, M., Compagnoni, R., 2009. The P-T path of the ultra-high pressure Lago Di Cignana and adjoining high-pressure meta-ophiolitic units: insights into the evolution of the subducting Tethyan slab. J. Metamorph. Geol. 27, 207–231. https://doi.org/10.1111/j.1525-1314.2009.00814.x.
Guillong, M., Meier, D., Allan, M., Heinrich, C., Yardley, B., 2008. SILLS: a MATLAB-based program for the reduction of laser ablation ICP-MS data of homogeneous materials and inclusions. Miner. Assoc. Can. Short Course 40.
Hein, J.R., Koschinsky, A., Halliday, A.N., 2003. Global occurrence of tellurium-rich ferromanganese crusts and a model for the enrichment of tellurium. Geochim. Cosmochim. Acta 67, 1117–1127. https://doi.org/10.1016/s0016-7037(02)01279-6.
Hermann, J., 2002. Allanite: Thorium and light rare earth element carrier in subducted crust. Chem. Geol. 192, 289–306. https://doi.org/10.1016/S0009-2541(02)00222-X.
Hermann, J., Spandler, C., Hack, A., Korsakov, A.V., 2006. Aqueous fluids and hydrous melts in high-pressure and ultra-high pressure rocks: implications for element transfer in subduction zones. Lithos 92, 399–417. https://doi.org/10.1016/j.lithos.2006.03.055.
Hulme, S.M., Wheat, C.G., Fryer, P., Mottl, M.J., 2010. Pore water chemistry of the Mariana serpentinite mud volcanoes: a window to the seismogenic zone. Geochem. Geophys. Geosyst. 11 https://doi.org/10.1029/2009GC002674@10.1002/(ISSN)1525-2027.IZUBONIN1.
Jochum, K.P., Nohl, U., Herwig, K., Lammel, E., Stoll, B., Hofmann, A.W., 2005. GeoReM: a new geochemical database for reference materials and isotopic standards. Geostand. Geoanal. Res. 29, 333–338. https://doi.org/10.1111/j.1751-908x.2005.tb00904.x.
Johnson, H.P., Hall, J.M., 1978. A detailed rock magnetic and opaque mineralogy study of the basalts from the Nazca Plate. Geophys. J. Int. 52, 45–64. https://doi.org/10.1111/j.1365-246X.1978.tb04221.x.
Kelley, K.A., Plank, T., Ludden, J., Staudigel, H., 2003. Composition of altered oceanic crust at ODP Sites 801 and 1149. Geochem. Geophys. Geosyst. 4 https://doi.org/10.1029/2002GC000435.
Kendall, B., Dahl, T.W., Anbar, A.D., 2017. Good Golly, Why Moly? The stable isotope geochemistry of molybdenum. In: Non-traditional Stable Isotopes. Walter de Gruyter GmbH, pp. 683–732. https://doi.org/10.2138/rmg.2017.82.16.
König, S., Münker, C., Schuth, S., Garbe-Schönberg, D., 2008. Mobility of tungsten in subduction zones. Earth Planet. Sci. Lett. 274, 82–92. https://doi.org/10.1016/j.epsl.2008.07.002.
König, S., Münker, C., Schuth, S., Luguet, A., Hoffmann, J.E., Kuduon, J., 2010. Boninites as windows into trace element mobility in subduction zones. Geochim. Cosmochim. Acta 74, 684–704. https://doi.org/10.1016/j.gca.2009.10.011.
König, S., Wille, M., Voegelin, A., Schoenberg, R., 2016. Molybdenum isotope systematics in subduction zones. Earth Planet. Sci. Lett. 447, 95–102. https://doi.org/10.1016/j.epsl.2016.04.033.
König, S., Rosca, C., Kurzawa, T., Varas-Reus, M.I., Dragovic, B., Schoenberg, R., John, T., 2021. Selenium isotope evidence for pulsed flow of oxidative slab fluids. Geochem. Perspect. Lett. 17, 27–32. https://doi.org/10.7185/geochemlet.2110.
Large, R.R., Maslennikov, V.V., Robert, F., Danyushevsky, L.V., Chang, Z., 2007. Multistage sedimentary and metamorphic origin of pyrite and gold in the Giant Sukhoi log deposit, Lena Gold Province, Russia. Econ. Geol. 102, 1233–1267. https://doi.org/10.2113/gsecongeo.102.7.1233.
Leeman, W.P., Tonarini, S., Turner, S., 2017. Boron isotope variations in Tonga-Kermadec-New Zealand arc lavas: implications for the origin of subduction components and mantle influences. Geochem. Geophys. Geosyst. 18, 1126–1162. https://doi.org/10.1002/2016GC006523.
Liang, Y.H., Halliday, A.N., Siebert, C., Fitton, J.G., Burton, K.W., Wang, K.L., Harvey, J., 2017. Molybdenum isotope fractionation in the mantle. Geochim. Cosmochim. Acta 199, 91–111. https://doi.org/10.1016/j.gca.2016.11.023.
McCoy-West, A.J., Chowdhury, P., Burton, K.W., Sossi, P., Nowell, G.M., Fitton, J.G., Kerr, A.C., Cawood, P.A., Williams, H.M., 2019. Extensive crustal extraction in Earth's early history inferred from molybdenum isotopes. Nat. Geosci. 12, 946–951. https://doi.org/10.1038/s41561-019-0451-2.
Menard, H.W., Natland, J., Jordan, T.H., Orcutt, J.A., et al., 1987. Site 595: Coring and Downhole Seismic Experiments in the Southwest Pacific Near the Tonga Trench., Initial Reports DSDP, Leg 91, Wellington to Papeete. US Govt. Printing Office; UK distributors, IPOD Committee, NERC, Swindon. https://doi.org/10.2973/dsdp.proc.91.102.1987.
Myeong, B., Kim, J., Kim, J.H., Jang, Y.D., 2020. Petrogenesis of subduction-related lavas from the southern Tonga arc. J. Asian Earth Sci. 188, 104089. https://doi.org/10.1016/j.jseaes.2019.104089.
Nägler, T.F., Neubert, N., Böttcher, M.E., Dellwig, O., Schnetger, B., 2011. Molybdenum isotope fractionation in pelagic euxinia: evidence from the modern Black and Baltic Seas. Chem. Geol. 289, 1–11. https://doi.org/10.1016/j.chemgeo.2011.07.001.
Peters, D., Pettke, T., 2017. Evaluation of major to ultra trace element bulk rock chemical analysis of nanoparticulate pressed powder pellets by LA-ICP-MS. Geostand. Geoanal. Res. 41, 5–28. https://doi.org/10.1111/ggr.12125.
Pettke, T., Oberli, F., Audétat, A., Guillong, M., Simon, A.C., Hanley, J.J., Klemm, L.M., 2012. Recent developments in element concentration and isotope ratio analysis of individual fluid inclusions by laser ablation single and multiple collector ICP-MS. Ore Geol. Rev. https://doi.org/10.1016/j.oregeorev.2011.11.001.
Plank, T., 2005. Constraints from Thorium/Lanthanum on sediment recycling at subduction zones and the evolution of the continents. J. Petrol. 46, 921–944. https://doi.org/10.1093/petrology/egi005.
Reinecke, T., 1991. Very-high-pressure metamorphism and uplift of coesite-bearing metasediments from the Zermatt-Saas zone, Western Alps. Eur. J. Mineral. 3, 7–18. https://doi.org/10.1127/ejm/3/1/0007.
Rudnick, R.L., Gao, S., 2014. Composition of the continental crust. In: Treatise on Geochemistry, Second ed. Elsevier Inc, pp. 1–51. https://doi.org/10.1016/B978-0-08-095975-7.00301-6.
Salters, V.J.M., Stracke, A., 2004. Composition of the depleted mantle. Geochem. Geophys. Geosyst. 5 https://doi.org/10.1029/2003GC000597 n/a-n/a.
Savov, I.P., Ryan, J.G., D'Antonio, M., Kelley, K., Mattie, P., 2005. Geochemistry of serpentinized peridotites from the Mariana Forearc Conical Seamount, ODP Leg 125: implications for the elemental recycling at subduction zones. Geochem. Geophys. Geosyst. 6 https://doi.org/10.1029/2004GC000777.
Savov, I.P., Ryan, J.G., D'Antonio, M., Fryer, P., 2007. Shallow slab fluid release across and along the Mariana arc-basin system: insights from geochemistry of serpentinized peridotites from the Mariana fore arc. J. Geophys. Res. Solid Earth 112. https://doi.org/10.1029/2006JB004749.
Schellart, W.P., Lister, G.S., Toy, V.G., 2006. A Late Cretaceous and Cenozoic reconstruction of the Southwest Pacific region: tectonics controlled by subduction and slab rollback processes. Earth Sci. Rev. 76, 191–233. https://doi.org/10.1016/j.earscirev.2006.01.002.
Schuth, S., König, S., Münker, C., 2011. Subduction zone dynamics in the SW Pacific plate boundary region constrained from high-precision Pb isotope data. Earth Planet. Sci. Lett. 311, 328–338. https://doi.org/10.1016/j.epsl.2011.09.006.
Seyfried, W.E., Shanks, W.C., Dibble, W.E., 1978. Clay mineral formation in DSDP Leg 34 basalt. Earth Planet. Sci. Lett. 41, 265–276. https://doi.org/10.1016/0012-821X(78)90183-8.
Siebert, C., Nägler, T.F., Kramers, J.D., 2001. Determination of molybdenum isotope fractionation by double-spike multicollector inductively coupled plasma mass spectrometry. Geochem. Geophys. Geosyst. 2 https://doi.org/10.1029/2000GC000124.
Siebert, C., Nägler, T.F., von Blanckenburg, F., Kramers, J.D., 2003. Molybdenum isotope records as a potential new proxy for paleoceanography. Earth Planet. Sci. Lett. 211, 159–171. https://doi.org/10.1016/S0012-821X(03)00189-4.
Skora, S., Freymuth, H., Blundy, J., Elliott, T., Guillong, M., 2017. An experimental study of the behaviour of cerium/molybdenum ratios during subduction: implications for tracing the slab component in the Lesser Antilles and Mariana Arc. Geochim. Cosmochim. Acta 212, 133–155. https://doi.org/10.1016/j.gca.2017.05.025.
Syracuse, E.M., van Keken, P.E., Abers, G.A., Suetsugu, D., Bina, C., Inoue, T., Wiens, D., Jellinek, M., 2010. The global range of subduction zone thermal models. Phys. Earth Planet. Inter. 183, 73–90. https://doi.org/10.1016/j.pepi.2010.02.004.
Tonarini, S., Leeman, W.P., Leat, P.T., 2011. Subduction erosion of forearc mantle wedge implicated in the genesis of the South Sandwich Island (SSI) arc: evidence from boron isotope systematics. Earth Planet. Sci. Lett. 301, 275–284. https://doi.org/10.1016/j.epsl.2010.11.008.
Tossell, J.A., 2005. Calculating the partitioning of the isotopes of Mo between oxidic and sulfidic species in aqueous solution. Geochim. Cosmochim. Acta 69, 2981–2993. https://doi.org/10.1016/j.gca.2005.01.016.
Turner, S., Hawkesworth, C., Rogers, N., Bartlett, J., Worthington, T., Hergt, J., Pearce, J., Smith, I., 1997. 238U-230Th disequilibria, magma petrogenesis, and flux rates beneath the depleted Tonga-Kermadec island arc. Geochim. Cosmochim. Acta 61, 4855–4884. https://doi.org/10.1016/S0016-7037(97)00281-0.
Ulmer, P., Trommsdorff, V., 1995. Serpentine stability to mantle depths and subduction-related magmatism. Science (80-.) 268, 858–861. https://doi.org/10.1126/science.268.5212.858.
Ulrich, T., Kamber, B.S., Woodhead, J.D., Spencer, L.A., 2010. Long-term observations of isotope ratio accuracy and reproducibility using quadrupole ICP-MS. Geostand. Geoanal. Res. 34, 161–174. https://doi.org/10.1111/j.1751-908X.2010.00046.x.
Villalobos-Orchard, J., Freymuth, H., O'Driscoll, B., Elliott, T., Williams, H., Casalini, M., Willbold, M., 2020. Molybdenum isotope ratios in Izu arc basalts: the control of subduction zone fluids on compositional variations in arc volcanic systems. Geochim. Cosmochim. Acta 288, 68–82. https://doi.org/10.1016/j.gca.2020.07.043.
Vitale-Brovarone, A., Groppo, C., Hetényi, G., Compagnoni, R., Malavielle, J., 2011. Coexistence of lawsonite-bearing eclogite and blueschist: phase equilibria modelling of Alpine Corsica metabasalts and petrological evolution of subducting slabs. J. Metamorph. Geol. 29, 583–600. https://doi.org/10.1111/j.1525-1314.2011.00931.x.
Voegelin, A.R., Pettke, T., Greber, N.D., von Niederhäusern, B., Nägler, T.F., 2014. Magma differentiation fractionates Mo isotope ratios: evidence from the Kos Plateau Tuff (Aegean Arc). Lithos 190–191, 440–448. https://doi.org/10.1016/j.lithos.2013.12.016.
Wang, Z., Becker, H., 2018. Molybdenum partitioning behavior and content in the depleted mantle: insights from Balmuccia and Baldissero mantle tectonites (Ivrea

Zone, Italian Alps). Chem. Geol. 499, 138–150. https://doi.org/10.1016/j.chemgeo.2018.09.023.
Wei, S.S., Wiens, D.A., van Keken, P.E., Cai, C., 2017. Slab temperature controls on the Tonga double seismic zone and slab mantle dehydration. Sci. Adv. 3, e1601755 https://doi.org/10.1126/sciadv.1601755.
Weis, D., Kieffer, B., Maerschalk, C., Barling, J., De Jong, J., Williams, G.A., Hanano, D., Pretorius, W., Mattielli, N., Scoates, J.S., Goolaerts, A., Friedman, R.M., Mahoney, J. B., 2006. High-precision isotopic characterization of USGS reference materials by TIMS and MC-ICP-MS. Geochem. Geophys. Geosys. 7 https://doi.org/10.1029/2006GC001283.
Willbold, M., Elliott, T., 2017. Molybdenum isotope variations in magmatic rocks. Chem. Geol. 449, 253–268. https://doi.org/10.1016/j.chemgeo.2016.12.011.
Willbold, M., Hibbert, K., Lai, Y.-J., Freymuth, H., Hin, R.C., Coath, C., Vils, F., Elliott, T., 2016. High-precision mass-dependent molybdenum isotope variations in magmatic rocks determined by double-spike MC-ICP-MS. Geostand. Geoanal. Res. 40, 389–403. https://doi.org/10.1111/j.1751-908X.2015.00388.x.
Wille, M., Nebel, O., Van Kranendonk, M.J., Schoenberg, R., Kleinhanns, I.C., Ellwood, M.J., 2013. Mo-Cr isotope evidence for a reducing Archean atmosphere in 3.46-2.76Ga black shales from the Pilbara, Western Australia. Chem. Geol. 340, 68–76. https://doi.org/10.1016/j.chemgeo.2012.12.018.
Wille, M., Nebel, O., Pettke, T., Vroon, P.Z., König, S., Schoenberg, R., 2018. Molybdenum isotope variations in calc-alkaline lavas from the Banda arc, Indonesia: assessing the effect of crystal fractionation in creating isotopically heavy continental crust. Chem. Geol. 485, 1–13. https://doi.org/10.1016/j.chemgeo.2018.02.037.
Yang, J., Siebert, C., Barling, J., Savage, P., Liang, Y.H., Halliday, A.N., 2015. Absence of molybdenum isotope fractionation during magmatic differentiation at Hekla volcano, Iceland. Geochim. Cosmochim. Acta 162, 126–136. https://doi.org/10.1016/j.gca.2015.04.011.
Yang, J., Barling, J., Siebert, C., Fietzke, J., Stephens, E., Halliday, A.N., 2017. The molybdenum isotopic compositions of I-, S- and A-type granitic suites. Geochim. Cosmochim. Acta 205, 168–186. https://doi.org/10.1016/j.gca.2017.01.027.
Zack, T., Kronz, A., Foley, S.F., Rivers, T., 2002. Trace element abundances in rutiles from eclogites and associated garnet mica schists. Chem. Geol. 184, 97–122. https://doi.org/10.1016/S0009-2541(01)00357-6.
Zhang, Y., Yuan, C., Sun, M., Li, J., Long, X., Jiang, Y., Huang, Z., 2020. Molybdenum and boron isotopic evidence for carbon-recycling via carbonate dissolution in subduction zones. Geochim. Cosmochim. Acta 278, 340–352. https://doi.org/10.1016/j.gca.2019.12.013.
Zhao, P.-P., Li, J., Zhang, L., Wang, Z.-B., Kong, D.-X., Ma, J.-L., Wei, G.-J., Xu, J.-F., 2016. Molybdenum mass fractions and isotopic compositions of international geological reference materials. Geostand. Geoanal. Res. 40, 217–226. https://doi.org/10.1111/j.1751-908X.2015.00373.x.
Zhou, L., Kyte, F.T., 1992. Sedimentation history of the South Pacific pelagic clay province over the last 85 million years Inferred from the geochemistry of Deep Sea Drilling Project Hole 596. Paleoceanography 7, 441–465. https://doi.org/10.1029/92PA01063.